EMA-97-R-010

EMA Electro Magnetic Applications, Inc.

P.O. Box 260263
Denver, CO 80226-0263
(303) 980-0070

LIGHTNING THREAT ANALYSIS FOR THE SPACE SHUTTLE LAUNCH PAD AND THE PAYLOAD CHANGEOUT ROOM USING FINITE DIFFERENCE METHODS

Prepared by:
Richard S. Collier

Prepared for:
NASA:
John F. Kennedy Space Center
Procurement Office OP-FED-1
Engineering Center RT-SRD-2
Kennedy Space Center, FL 32899

MAY 15, 1997

National Aeronautics and
Space Administration

John F. Kennedy Space Center

TABLE OF CONTENTS

TABLE OF FIGURES

CHAPTER 1

INTRODUCTION

The purpose of this report is to describe finite difference computer calculations for the Space Shuttle Launch Pad which predict lightning induced electric currents and electric and magnetic fields caused by a lightning strike to the Lightning Protection System (LPS) catenary wire. Description of possible lightning threats to Shuttle Payload components together with specifications for protection of these components, result from the calculation of lightning induced electric and magnetic fields inside and outside the Payload Changeout Room (PCR) during a lightning event. These fields also induce currents and voltages on cables and circuits which may be connected to, or a part of, shuttle payload components. These currents and voltages are also calculated. These threat levels are intended as a guide for designers of payload equipment to specify any shielding and/or lightning protection mitigation which may be required for payload components which are in the process of preparation or being transferred into the Shuttle Orbiter. Other critical interior spaces considered in this report include the White Room at Orbiter cabin door (Chapter 7) and also the interior of the Orbiter payload bay (Chapter 6).

The calculated response at any point in or around the Space Shuttle launch pad depends on the amplitude, the risetime and frequency content of the lightning waveform and also the attach point of the lightning strike. Most lightning strikes attach to the catenary. In this case, currents on the structure are induced by electromagnetic fields – so called "indirect" effects. Some strikes may bypass the catenary and attach to the launch pad structure. An example of direct attachment (or "direct" effects) to the structure is included as a computer model of a direct strike which attached to the PCR framework on June 25, 1994 (Chapter 5).

Since the Launch Pad structure is large and made primarily of metals, there are natural electromagnetic resonances (akin to the "ringing" of a bell) which are exited by strong spectral components of the lightning waveform. These resonances can have very high amplitudes, and are manifest by high amplitude oscillating fields and currents in and around the structure. These resonance effects are discussed (Chapter 8). The effects of the waveforms on the resonance responses are seen throughout this report; waveforms with faster risetimes excite the higher frequency resonance modes.

There is always the question of "how good" are the calculations. The calculated response depends on a number of factors including the modeling itself, the lightning amplitude and waveform, and the point of attachment. Data comparisons of the calculations with a lightning simulator experiment conducted in 1992 and direct monitoring of natural lightning strikes will be discussed in a future joint report with EMA, NASA and Lightning Technologies Inc. However, preliminary comparisons between the computer model and experimental data show that agreement in field amplitudes may well be within a factor of 2 or 3; there is also some limited data which shows correlation in the spectral resonance frequencies as predicted by the model and measured experimentally. It is anticipated that comparison of the model with this and future experiments will result in more precise evaluations and possible improvements of the model.

Since experimental data related to simulated or natural lightning events is relatively hard to come by, it appears that the model calculations will be useful not only in predicting threat levels in and around the Launch Pad structure – but will be useful also in extrapolating experimental data, usually taken at a point, to various other parts of the structure. The calculations also make it easier to investigate the effect of variations in the lightning amplitudes, risetimes and waveforms and also the possible points of attachment. Transfer function techniques are discussed (Chapter 8) which may be used to investigate variations in responses for various waveforms without the necessity of redoing the entire numerical calculation for each waveform – this can be done for each lightning attach point which may be of interest. Transfer functions may also be developed to relate data from experimental observation points to critical locations within the PCR. This analysis could provide useful data to evaluate the need for possible re-testing of payload components which may have been present during a lightning strike.

The remainder of this report will be concerned primarily with the modeling and calculation techniques and some of the calculated results.

CHAPTER 2

THE FINITE DIFFERENCE COMPUTER MODEL

2.1 Introduction

The numerical model of the space shuttle Launch Pad Structure and surrounding environment is based upon a finite difference time domain solution of Maxwell's Equations. The solution technique is explicit and accurate to second order in the time and spatial increments, which in these models correspond to the three dimensional cartesian coordinate increments as obtained by Merewether and Fisher [1].

A finite problem space containing and surrounding the Launch Pad environment is broken up into rectangular cells. The fields calculated by Maxwell's Equations are equivalent to the average value of the electric and magnetic fields which occupy the cell. The number and size of the cells are determined by the size of the problem space, the available computer memory and speed of the computer, and the desired frequency bandwidth of the solution, which for lightning problems should be on the order of 20 MHz or somewhat greater. The cell size also dictates the time increment for time stepping the solution for the entire problem space. The time increment gets shorter for smaller cell sizes, hence there is a practical computational limit as to how small the cells can be made. The solutions described herein are obtained using a CRAY II computer. For these problems there are typically .1 to 1 million cells in the problem space. The cell sizes range from .25 to 1 meter and the solutions as obtained by the CRAY II computer give about 1 microsecond of calculated lightning response for each approximately 10 to 30 minutes of CPU computing time. The fields, currents and voltages are calculated for each cell in the problem space as functions of time for time steps on the order of 2 nanoseconds or somewhat less. Fields, currents and voltages are saved at desired test point locations and written to computer files for use in display and analysis of data.

2.2 The Staggered Spatial Grid for Electric and Magnetic Fields

A problem space containing the facility and surrounding environment is divided into rectangular cells. Each cell has a staggered spatial grid, as shown in figure 2.1, composed of the vector components of E and H. The cell dimensions Δx, Δy and Δz are 1 meter for the external launch pad coupling problem and .5 meter and .25 meter for the internal PCR coupling problem.

The field components in each cell are calculated numerically via the finite difference form of Maxwell's Equations [1].

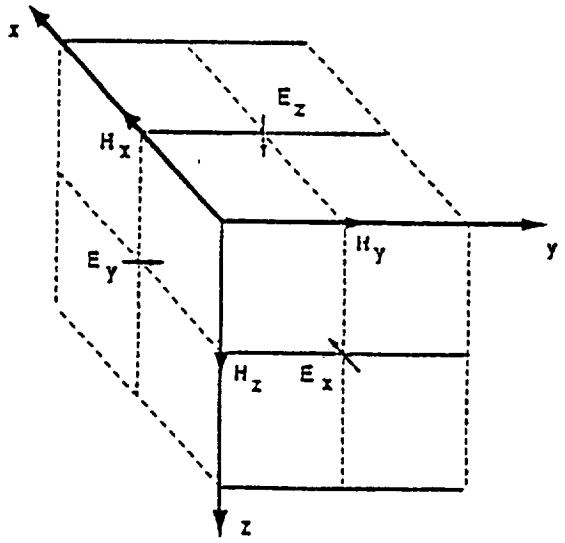

MAXWELL'S EQUATIONS

$$\mu\frac{\partial H}{\partial t} + \nabla\times E = M \qquad (2.1)$$

$$\epsilon\frac{\partial E}{\partial t} + \sigma E - \nabla\times H = -J \qquad (2.2)$$

$$\nabla \cdot E = \frac{\rho}{\epsilon} \qquad (2.3)$$

$$\nabla \cdot H = 0 \qquad (2.4)$$

Figure 2.1 **Staggered Spatial Grid**

The vector components of equations 2.1 and 2.2 describing the time advance of magnetic and electric fields respectively are shown in figure 2.2 together with the centered finite difference formulation of these equations. It is seen that besides being staggered in space, the electric and magnetic fields are also staggered in time. the numbers MX, MY and MZ are the numbers of cells in the X, Y and Z directions respectively.

The time step (increment) for this finite difference solution of Maxwell's Equations is determined by the Courant criterion, which may be viewed as requiring that the speed of numerical propagation be greater than the fastest physical wave speed, in this case the speed of light in air. Specifically, the Courant condition is:

$$\Delta t \le \frac{1}{c\sqrt{\frac{1}{\Delta x^2} + \frac{1}{\Delta y^2} + \frac{1}{\Delta z^2}}} \qquad (2.5)$$

where Δt is the time step, Δx, Δy, and Δz are the three cartesian spatial increments and c is the speed of light in the air. For the external coupling problem Δt is 1.8×10^{-9} sec and for the internal coupling problems Δt .45 to is.9 x 10^{-9} sec. The smallest spatial increments control the time step,

Finite Difference Formulation of Maxwell's Equations. Reference [1]

Assumptions: None

Maxwell's Equations

$$-\mu\left(\frac{\partial H_x}{\partial t}\right) = \left(\frac{\partial E_z}{\partial y}\right) - \left(\frac{\partial E_y}{\partial z}\right) \qquad H_x^n(i,j,k) = H_x(x(i), y_O(j), z_O(k), t_H(n))$$

$$-\mu\left(\frac{\partial H_y}{\partial t}\right) = \left(\frac{\partial E_x}{\partial z}\right) - \left(\frac{\partial E_z}{\partial x}\right) \qquad H_y^n(i,j,k) = H_y(x_O(i), y(j), z_O(k), t_H(n))$$

$$-\mu\left(\frac{\partial H_z}{\partial t}\right) = \left(\frac{\partial E_y}{\partial x}\right) - \left(\frac{\partial E_x}{\partial y}\right) \qquad H_z^n(i,j,k) = H_z(x_O(i), y_O(j), z(k), t_H(n))$$

$$\varepsilon\frac{\partial E_x}{\partial t} + \sigma E_x = \left(\frac{\partial H_z}{\partial y}\right) - \left(\frac{\partial H_y}{\partial z}\right) - i_x \qquad E_x^n(i,j,k) = E_x(x_O(i), y(j), z(k), t_E(n))$$

$$\varepsilon\frac{\partial E_y}{\partial t} + \sigma E_y = \left(\frac{\partial H_x}{\partial z}\right) - \left(\frac{\partial H_z}{\partial x}\right) - i_y \qquad E_y^n(i,j,k) = E_y(x(i), y_O(j), z(k), t_E(n))$$

$$\varepsilon\frac{\partial E_z}{\partial t} + \sigma E_z = \left(\frac{\partial H_y}{\partial x}\right) - \left(\frac{\partial H_x}{\partial y}\right) - i_z \qquad E_z^n(i,j,k) = E_z(x(i), y(j), z_O(k), t_E(n))$$

$x_O(i) = (i-1)\Delta x$, $y_O(j) = (j-1)\Delta y$, $z_O(k) = (k-1)\Delta z$, $t_H(n) = (n-1)\Delta t$

$x(i) = (i-1/2)\Delta x$, $y(j) = (j-1/2)\Delta y$, $z(k) = (k-1/2)\Delta z$, $t_E(n) = (n-1/2)\Delta t$

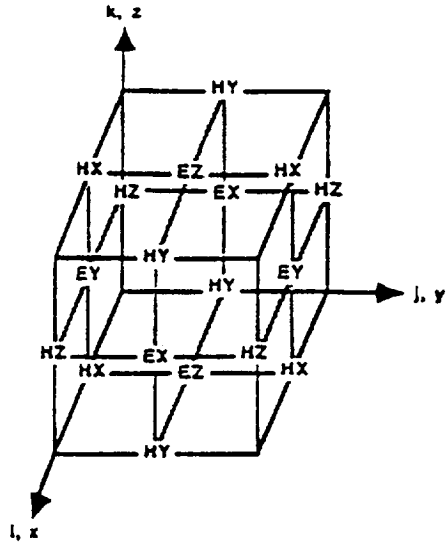

Finite Difference Equations (non-uniform grid allowed)

$$H_x^{n+1}(i,j+1,k+1) = H_x^n(i,j+1,k+1) - \frac{\Delta t}{\mu}\left(\frac{E_z^n(i,j+1,k+1) - E_z^n(i,j,k+1)}{y(j+1) - y(j)}\right) + \frac{\Delta t}{\mu}\left(\frac{E_y^n(i,j+1,k+1) - E_y^n(i,j+1,k)}{z(k+1) - z(k)}\right) \qquad \begin{cases} i\in[1,MX-1] \\ j\in[1,MY-2] \\ k\in[1,MZ-2] \end{cases}$$

$$H_y^{n+1}(i+1,j,k+1) = H_y^n(i+1,j,k+1) - \frac{\Delta t}{\mu}\left(\frac{E_z^n(i+1,j,k+1) - E_z^n(i+1,j,k)}{z(k+1) - z(k)}\right) + \frac{\Delta t}{\mu}\left(\frac{E_x^n(i+1,j,k+1) - E_x^n(i,j,k+1)}{x(i+1) - x(i)}\right) \qquad \begin{cases} i\in[1,MX-2] \\ j\in[1,MY-1] \\ k\in[1,MZ-2] \end{cases}$$

$$H_z^{n+1}(i+1,j,k) = H_z^n(i+1,j+1,k) - \frac{\Delta t}{\mu}\left(\frac{E_y^n(i+1,j+1,k) - E_y^n(i,j+1,k)}{x(i+1) - x(i)}\right) + \frac{\Delta t}{\mu}\left(\frac{E_x^n(i+1,j+1,k) - E_x^n(i+1,j,k)}{y(j+1) - y(j)}\right) \qquad \begin{cases} i\in[1,MX-2] \\ j\in[1,MY-2] \\ k\in[1,MZ-1] \end{cases}$$

$$B\text{-}E_x^{n+1}(i,j,k) = A\text{-}E_x^n(i,j,k) - i_x(i,j,k) + \left(\frac{H_z^{n+1}(i,j+1,k) - H_z^{n+1}(i,j,k)}{y_O(j+1) - y_O(j)}\right) - \left(\frac{H_y^{n+1}(i,j,k+1) - H_y^{n+1}(i,j,k)}{z_O(k+1) - z_O(k)}\right) \qquad \begin{cases} i\in[1,MX-1] \\ j\in[1,MY-1] \\ k\in[1,MZ-1] \end{cases}$$

$$B\text{-}E_y^{n+1}(i,j,k) = A\text{-}E_y^n(i,j,k) - i_y(i,j,k) + \left(\frac{H_x^{n+1}(i,j,k+1) - H_x^{n+1}(i,j,k)}{z_O(k+1) - z_O(k)}\right) - \left(\frac{H_z^{n+1}(i+1,j,k) - H_z^{n+1}(i,j,k)}{x_O(i+1) - x_O(i)}\right) \qquad \begin{cases} i\in[1,MX-1] \\ j\in[1,MY-1] \\ k\in[1,MZ-1] \end{cases}$$

$$B\text{-}E_z^{n+1}(i,j,k) = A\text{-}E_z^n(i,j,k) - i_z(i,j,k) + \left(\frac{H_y^{n+1}(i+1,j,k) - H_y^{n+1}(i,j,k)}{x_O(i+1) - x_O(i)}\right) - \left(\frac{H_x^{n+1}(i,j+1,k) - H_x^{n+1}(i,j,k)}{y_O(j+1) - y_O(j)}\right) \qquad \begin{cases} i\in[1,MX-1] \\ j\in[1,MY-1] \\ k\in[1,MZ-1] \end{cases}$$

where $A = \left(\frac{\varepsilon}{\Delta t} - \frac{\sigma}{2}\right)$, $B = \left(\frac{\varepsilon}{\Delta t} + \frac{\sigma}{2}\right)$, $i_x(i,j,k) = i_x(x_O(i), y(j), z(k), t_H(n+1/2))$, $i_y(i,j,k) = i_y(x(i), y_O(j), z(k), t_H(n+1/2))$, $i_z(i,j,k) = i_z(x(i), y(j), z_O(k), t_H(n+1/2))$

Figure 2.2 Arrangement of Field Components on Unit Cell for Three Dimensional Staggered Finite Difference Mesh

but the largest spatial increments determine the bandwidth of the solution. The rule of thumb used is that the upper frequency bandwidth limit of the solution, f_{max}, is given by

$$f_{max} = \frac{c}{8_{max}(\Delta x, \Delta y, \Delta z)}$$

For the launch pad model discussed here, this corresponds to a bandwidth of about 37 MHz, which is more than sufficient to describe the worst case lightning environment scenario.

Maxwell's curl Equations (2.1), (2.2) form a system of hyperbolic partial differential equations which not only require initial conditions at all spatial locations, but also the boundary values of the electromagnetic field components (or their normal derivatives) at all times to obtain a well posed solution. These values must be supplied at the boundaries of the computational volume by an appropriate termination condition. The boundary condition employed was derived by Mur [2], and is essentially a first order integration along outgoing (with respect to the interior of the computational volume) characteristics. That is, the characteristic direction is chosen to be causal in time and along the outward normal to the bounding surface, which is a two dimensional cartesian coordinate plane. Boundary conditions also must be imposed on metallic surfaces such as the door, interior wall and metal equipment. The boundary condition on metal surfaces at least as large as a cell face is that the tangential electric fields at the surfaces of the metallic objects are set equal to zero each time step. Although this is correct only for perfect electrical conductors, on the time scale of interest, it is an excellent approximation.

If the Maxwell divergence Equations (2.3), (2.4) are satisfied at the initial time step then the finite difference time development of the curl equations automatically satisfy the divergence equations at each time step. Thus the static solution in the problem space satisfying (2.3) and (2.4) is tantamount to specifying the initial conditions for the problem. The simplest initial condition is to set $E = H = \rho = 0$ throughout the problem space. However, physically, a lightning discharge is normally a dynamic release of a static field buildup ("pre-polarization") between the cloud and ground. The Launch Pad Structure will cause local static field enhancements from the pre-polarization between cloud and ground. The air dielectric breakdown will then usually occur at the point of highest electric field, e.g., the catenary cable or protrusion of the structure.

Thus it is sometimes necessary to obtain the initial static solution for the facility under high pre-polarization field conditions in order to faithfully track the fields and currents of the resulting lightning strike. At other times it may be sufficient to realize that under linear conditions and a given lightning or experimental current injection waveform, the final solution is the superposition of the initial static solution and a dynamic solution with the initial fields and charge density set to zero. This report will be primarily concerned with the dynamic part of the solution under zero initial conditions.

In addition to the appropriate boundary and initial conditions, the material properties at each cell location must be specified. This consists of the magnetic permeability, μ, in Equation (2.1); the conductivity, σ, in Equation (2.2) and the dielectric constant, ε, in Equations (2.2) and (2.3). If the material is homogeneous within the cell (for example, volumes of air, soil, concrete, etc.) then the appropriate values of μ, σ, and ε are included in the time advance equations for the cell in question.

If the material properties are inhomogeneous in each cell (detailed structure, etc.) then a decision must be made on how to represent the properties in each cell. In some cases average properties are sufficient and in other cases they are not. Special considerations are available for treating apertures in metal walls and also for pipes and thin wires (radii much smaller than cell dimensions) which may run throughout the problem space. These pipes and wires can be carriers of high current. Most facilities of interest including the Launch Pad Structure and PCR interior usually have a great deal of "thin wire" situations in the form of signal and power lines, rebar in reinforced concrete, pipes, plumbing, metal poles, the lightning protection cables and underground return paths, etc. Methods for inserting "small" objects (e.g. wires, apertures) into the finite difference problem space will be described in Chapter 3.

2.3 Lightning Excitation and Input Waveforms

The Maxwell Equations are driven by the current density, J in Equation (2.2), by including J in the cells which are assumed to contain the Lightning Channel. The location of the lightning channel and attach point to the catenary cable are inputs to the numerical problem. The time dependent waveform for J may be taken from measured catenary currents due to natural lightning events or from lightning simulation experiments. Theoretical statistical bounds to investigate upper limits for the lightning threat at given test point locations may be obtained from the NSTS Standard Waveforms [11] (see also Figure 6.4). The NSTS waveforms which are typically double

exponential time dependent waveforms may be inserted directly for J in Equation 2.2 and its numerical counterpart for an assumed lightning channel and attach point. The channel and attach points for natural lightning could be taken from video images of the lightning event coupled with current measurements taken at the North and South ends of the Catenary wire to complete the description of lightning input excitation.

CHAPTER 3

THIN WIRES AND APERTURES

3.1 Introduction

Thin wires and apertures can have strong influence on local fields and currents but have one or more physical dimensions which are much less than the established size of the underlying finite difference cell. In most of these instances, if the cell size were decreased to accommodate the size of these objects, extremely large numbers of cells would be necessary to fill the problem space resulting possibly in extreme, if not impossible, use of computer time and memory. It is sometimes useful to use limited subgrids (smaller cell sizes) in some regions of the problem space in connection with these objects; however, this also increases the number of needed time steps for the total problem. In other cases described in this chapter, self-consistent approximation techniques are utilized which embed these smaller wires and apertures into the normal finite difference grid.

The thin wire formalism is used to describe the overhead catenary wire, the grounding straps between the Orbiter and the PCR in the Mate position and also drag-on cables which may connect Payloads in the Orbiter Bay with service equipment in the PCR interior. Thin wires are also used to model the ground straps between the White Room and the Orbiter at the location of the Orbiter Cabin door.

Apertures provide the primary coupling (or points of entry, POE's, for electromagnetic energy) between the interior spaces of the structure and the exterior lightning environment. Theses interior spaces include the PCR interior, the Orbiter payload bay and the Orbiter Cabin Access Walkway including the White Room at the interface of the Walkway and the Orbiter Cabin. For each of these cases the apertures appear at the non-metallic inflatable seals between the metallic mating surfaces and also along the gaps in seams at the door edges.

3.2 Thin Wires

The thin wires, cables and rods are implemented in a self-consistent fashion by making use of the telegrapher's transmission line equations. The telegrapher's Equations (3.1), (3.2) are a one

dimensional solution of Maxwell's in terms of currents, I_w, and voltages, V_w, on the wires, which are required to have diameters less than cell size (spatial increment). The per unit length inductances and capacitances are defined (3.3), (3.4) with respect to the cell size and the wire diameter, 2a.

One Dimensional Transmission Line Equations:

$$\frac{\partial V_w}{\partial Z} = -L_w \frac{\partial I_w(K)}{\partial t} - I_w R_w + Ez(i_w, j_w, k) \tag{3.1}$$

$$\frac{\partial I_w}{\partial Z} = -C_w \frac{\partial V_w}{\partial t} - G_w V_w \tag{3.2}$$

where L_w and C_w is the in-cell inductance and capacitance of the wire per unit length.

$$L_w = \frac{\mu l}{2\pi} \ln\left(\frac{\Delta y}{2a}\right) \tag{3.3}$$

$$C_w = \frac{2\pi a \epsilon E_r(a)}{V_w} = \frac{2\pi\epsilon}{\ln\left(\frac{\Delta y}{2a}\right)} \tag{3.4}$$

G_w is the in-cell conductance from the wire to the surrounding conductive medium

$$G_w = \frac{\sigma}{\epsilon} C_w \tag{3.5}$$

The wire resistance per unit length, R_w, is obtained by considering the surface conduction of the metal in question using the skin depth obtained for a frequency of 1 MHz. The resistance

for pipes, wire, iron rebar, etc., is normally on the order of 10^{-3} Ohms/meter. In practice, the major results at early time seem to be relatively insensitive to variations of the resistance.

In the computer code, the wires and pipes are embedded into the staggered grid and are driven by the electric field component (see Equation (3.1)) calculated by the three dimensional solution of Maxwell's Equations. In order to maintain electrical charge conservation, this wire current must also be injected back into the driving electric field component as a source current via Maxwell's Equation (2.2). At the interconnections, which are voltage nodes, Kirchoff's law is invoked. At locations where the wires are situated in the soil or concrete, the wires are in electrical contact with the soil or concrete with in-cell conductance given by G_w in Equation (3.5). This is also true of the ground wires which are in contact with the soil.

Complex networks of thin wires (e.g., metal rebar mesh embedded in conducting concrete) are included in the model by a vectorized extension of the transmission line formalism. Vectorized average wire currents coincide with the electric field vectors in each cell and a corresponding average inductance and resistance is associated with each wire current vector. Six component tensors exist at the cell corners (nodes) describing the equivalent transmission line voltages, wire capacitance, and conductance to the embedding medium. A 36 component connectivity tensor exists at each node describing the ways that wires are connected at the nodes.

At the boundaries of the problem space, some termination condition must be applied to both cable extensions and the power and signal lines and metal pipes entering the problem space. The boundary condition is applied at current nodes and is the equivalent of the Mur boundary condition applied to the magnetic fields [2].

3.3 Apertures

The electromagnetic coupling through apertures is calculated using the method of "aperture polarizabilites" as described in Chapter 12 of the handbook on Lightning Protection of Aircraft by Fisher, Perala and Plummer [3]. Dalke [4] developed the algorithms for including the aperture polarizabilites into the framework of finite difference calculations using the Maxwell Equatations

According to Dalke [4], external electric and magnetic fields at the aperture, E and H respectively, generate equivalent electric and magnetic dipole currents, at the center of the

aperture, Ie and Im respectively. To a first approximation, these dipole currents are proportional to the time derivatives of the electric and magnetic fields respectively, given by

$$Ie = \epsilon \, Pe(dE/dt)/dz \tag{3.6}$$

and

$$Im = \mu \, Pm(dH/dt)/dz \tag{3.7}$$

where dz is the cell dimension in a direction normal to the plane of the aperture; E and H are taken to be average external fields over the aperture, or for simplicity, the fields at the aperture center. The proportionality constants Pe and Pm are called the electric and magnetic polarizabilities respectively, both with units expressed in cubic meters. These electric and magnetic dipole currents are translated into electric and magnetic current densities, J and M respectively, where

$$J = Ie/(dxdy) \tag{3.8}$$

and

$$M = Im/(dxdy \tag{3.9}$$

where dx and dy are cell dimensions in the plane of the aperture. These expressions for J and M are the source currents which drive Maxwell's Equations (2.1) and (2.2) being solved numerically for the interior space coupled by the aperture to the exterior lighting environment. The aperture is normally considered to be totally absorbing, that is, the generated internal fields normally are considered to have negligible effect on the magnitudes and waveforms of the external fields. Thus the external fields act as drivers for the internal fields.

The polarizabilities depend on the vector components of the external field and the size and shape of the aperture. For long narrow slits of length l, and width, w, Table 12.1 of the reference [3] shows the significant components of the polarizabilities to be

$$Pez = \pi \, w^2 l/16 \tag{3.10}$$

$$Phn = \pi \, w^2 l/16 \tag{3.11}$$

$$Php = (\pi/24) \, l^3 \, / \, (\ln(4l/w)-1) \tag{3.12}$$

where Pez is the electric field polarizability for the electric field normal to the aperture; Phn is the magnetic field polarizability for the magnetic field tangential to the aperture but normal to the long dimension of the slit; Php is the magnetic field polarizability for the magnetic field parallel to the long dimension of the slit. These values are calculated explicitly for the various applications and used to calculate the coupling using equations 3.6 to 3.9. Comparison of these values shows the stongest coupling to be due to magnetic fields which are parallel to the long length of the slits. This may be viewed heuristically as parallel magnetic field lines "squeezing" through the slit. Another point of view is that the parallel magnetic field at the surface (expressed in Amps per meter) represents a linear surface current density which is normal to the long dimension of the slit. This normal current is then driven into the interior through the discontinuity of the slit. These, plus dipole visualizations of apertures are shown in Figure 3.1 [3].

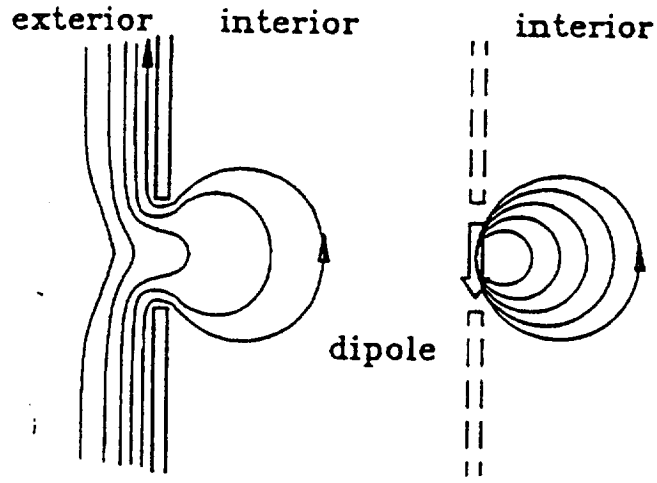

Fig. 12.2 Development of equivalent magnetic field dipole.
(a) Actual magnetic field
(b) Equivalent dipole

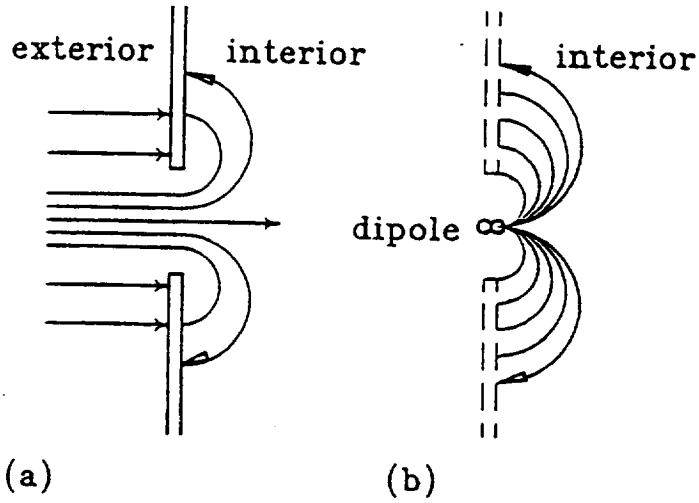

Fig. 12.1 Development of equivalent electric field dipole.
(a) Actual electric field
(b) Equivalent dipole

Figure 3.1 Dipole Representations of Apertures, Ref [3].

CHAPTER 4

LIGHTNING SIMULATION IN THE PARK POSITION

4.1 Introduction

In the park position, the Rotating Service Structure (RSS) is rotated back from the launch pad position to the opposite side of the catenary wire. The angle which the PCR face makes with the north-south line of the catenary wire was taken to be 45 degrees. The external elements of the RSS, PCR, and Fixed Service Structure (FSS) are established as perfect metals on a 1 meter grid. The internal structure inside the PCR is established on a .5 meter grid. The PCR main doors are closed. The energy transfer to the PCR interior is assumed to be through the 3/4 inch seam gaps around the main doors which are filled with an insulating gasket material. The coupling model, therefore, assumes long, narrow slits at the seam locations which are treated as apertures. The apertures are driven by surface currents on the PCR exterior which are normal to the seams and to some extent the surface charge residing at the seams. The normal surface currents are equivalent to the PCR tangential magnetic fields which are parallel to the seams. The surface charge density at the seam is given by the PCR exterior normal electric fields at the seams.

The model, as calculated in this chapter, is driven by the amplitude and waveform of the current generated by the lightning simulator which was connected to the north end of the catenary wire. The current on the catenary wire is calculated independently using current measurements at the south end of the catenary wire, at the CWLIS location, and at the north end at the simulator location. Assumptions were made with respect to visually observed arcing and other non-linear phenomenon. The current waveform on the catenary wire was also found experimentally and theoretically to be closely represented by magnetic field measurements taken on the exterior roof of the PCR [6]. By combining these measurements and calculations, the current amplitude and waveform was established for the simulator current on the catenary wire at the locations nearest to the PCR exterior.

The established simulator current was injected into the model in a unidirectional manner along the catenary wire. The resulting electric and magnetic fields were calculated external and internal to the PCR. Fields at test point locations are compared with experimentally obtained values. The agreement between the experimental and theoretical fields is reasonably good, to within a factor of 2 in most cases. Extension of these theoretical and experimental results from

the lightning simulator experiment to NSTS waveforms and possible lightning events is described in Chapter 8 using transfer function methods and frequency spectral analysis.

4.2 External Finite Difference Gridding

The problem space exterior to the PCR is constructed with cubical cells 1 meter on each side. Each cell side has two tangential components of the electric field. If a cell side coincides with a metal surface in the problem space, then the two tangential components of the electric field on the cell side in question are set equal to zero at each time step - in the approximation of perfect conductivity.

In the graphical representation of the structure it is sufficient to indicate the fields which are set to zero by drawing an elongated box surrounding the zeroed e-field. This is the staggered grid representation. Sometimes, for bulky metal objects, it is sufficient to simply draw in the cells for which all the e-field components are set to zero. This is the cell representation. In this report, sheets of metal (with air on each side), which are not completely closed, are drawn in the staggered grid representation. Long narrow poles and beams with lateral dimensions on the order of a cell size are also represented in the staggered grid representation as a long line of zeroed e-fields.

In the graphical figures, both staggered and cell representations are used, sometimes in the same figure. The external representation of the Launch Pad Structure in the Park Position is shown in Figure 4.1. The PCR and FSS elevator and crane are shown in the cell representation. The other surfaces and struts are shown in the staggered grid representation. For the Park calculation, a perfectly conducting ground plane is used which intersects the footings of the FSS and RSS. (The ground plane is not shown.) Figure 4.2 shows a larger representation of the closed PCR, the top building structures and the bottom skirt beneath the PCR.

In this representation, the PCR is rotated back so the front face of the PCR is at an angle of 45 degrees from the horizontal line projection of the catenary wire. Since this work was completed, it was determined that the retraction for the simulator experiment was 30 degrees, so the field components with respect to the PCR may vary somewhat with rotation angle. However, the total magnetic field at the PCR door center, which is generated by currents on the catenary wire, is expected to be about the same for the two retraction angles. Data comparisons between the calculations and experiment for the total magnetic field at the door center.

Figure 4.1 Launch Pad Structure in the Park Position

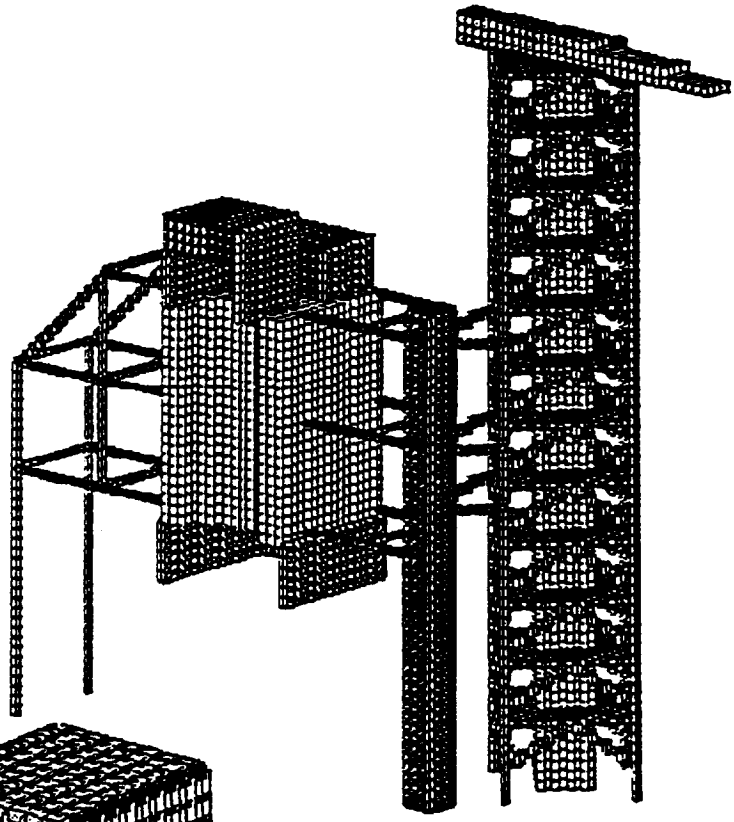

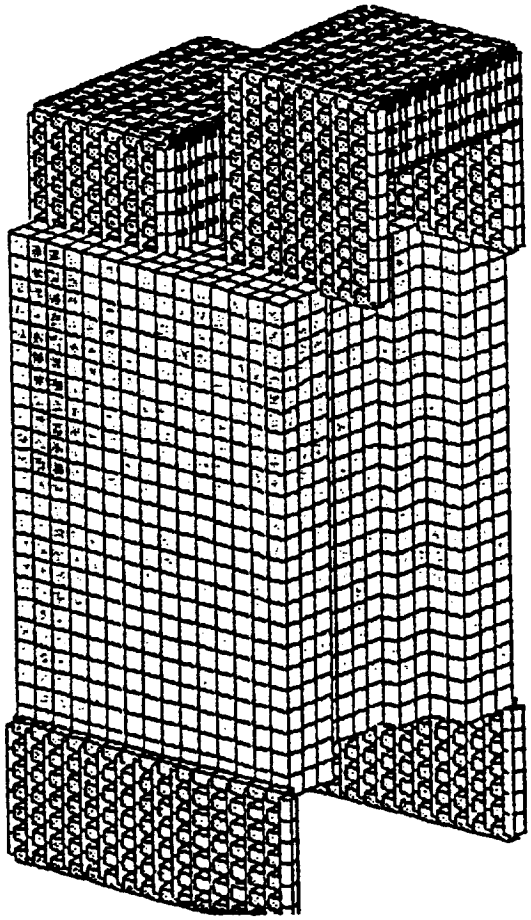

Figure 4.2 Closed PCR and Attached Metal Surfaces

4.3 Simulator Currents on the Catenary Wire

The Lightning Simulation Experiment (1992 at Launch Pad A) is adequately described elsewhere [5][6][7]. We note here that the experimental setup is shown in Figure 4.3 with the portable Marx Generator (on a flatbed trailer) inserted electrically in series with the LPS catenary wire at the north end. It was necessary to calculate the current on the catenary wire using measured currents at the Marx Generator and at the CWLIS location at the south end of the catenary. These calculations were made using a finite difference model of Figure 4.3 using a 10 meter grid; and were complicated by the existence of an arcing current of unknown amplitude and waveform which formed between the catenary and the ground shortly after the firing of the Generator. Of primary interest is the catenary current waveform above and in the vicinity of the PCR. The current is not uniform along the catenary wire because of the incident pulse on the north end traveling approximately 2000 feet along the catenary to the south end added to the pulse reflection back along the catenary from the south end. Several models were obtained for the catenary current waveform in the vicinity of the PCR and two examples are shown in Figure 4.4. for simulator run 24. The calculated current depends on the simulator input current and several assumed parameters, including the assumed time delay of the arcing, the effective resistance in the arc path, and some degree of "smoothing" due to corona discharge. For each set of parameters, the calculated current has a different amplitude and waveform.

4.4 Data Comparison of External Magnetic Field at PCR Door Center

Each of the calculated catenary currents were used as source currents for independent finite difference computer runs. The response anywhere in the problem space depends directly on the amplitude and waveform of the source current. For each of the currents, the total magnetic field was calculated at the PCR door center. These calculations were compared with the total magnetic field data for Run 24 which was measured as the vector sum of three independent measurements of the magnetic field components [5][6][7]. The comparisons are shown in Figure 4.5 corresponding to currents shown in Figure 4.4. The waveforms have the same general trend; the highly smoothed input waveform predicts oscillating components superimposed on the general waveform which are not apparent experimentally. The oscillations are likely due to the spectral frequency content of the calculated current input waveforms, which couple to resonance modes of the structure. These comparisons are not so much a test of the finite difference model itself as a combination of the model and the form used for the unknown experimental input waveform. The differences in the waveform comparisons at the PCR door center are apparently due to differences

in the calculated input waveforms. However, considering that either of the calculated input currents (shown in Fig 4.4) are "reasonable", the agreement between calculation and experiment appears to be well within a factor of 2 in peak amplitude. The amplitude of the resonance oscillations seen in the calculated results needs further investigation which can only be tested with further experimental data. These experimental comparisons would be expected to verify the amplitude of the resonances and any possibly suggest any additional damping factors which may be needed in the model.

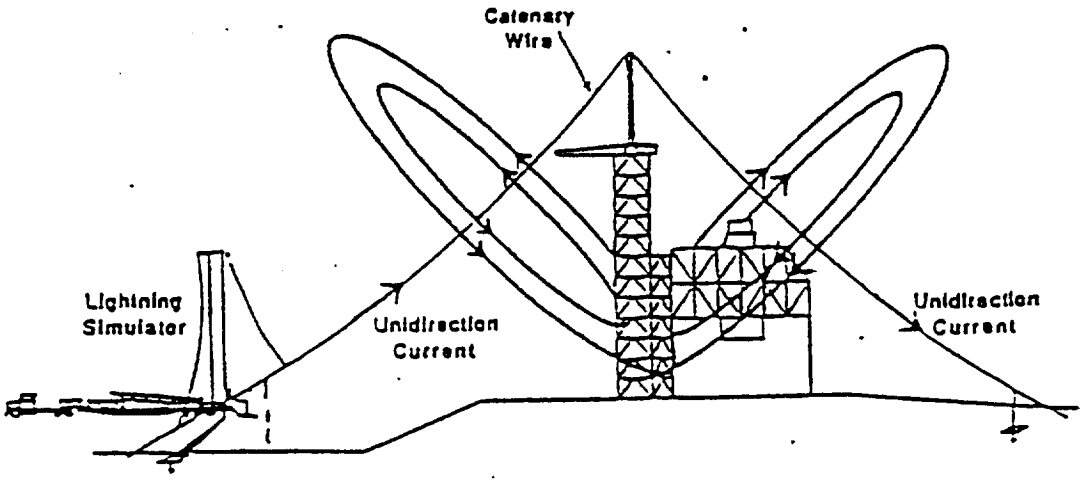

Test Configuration

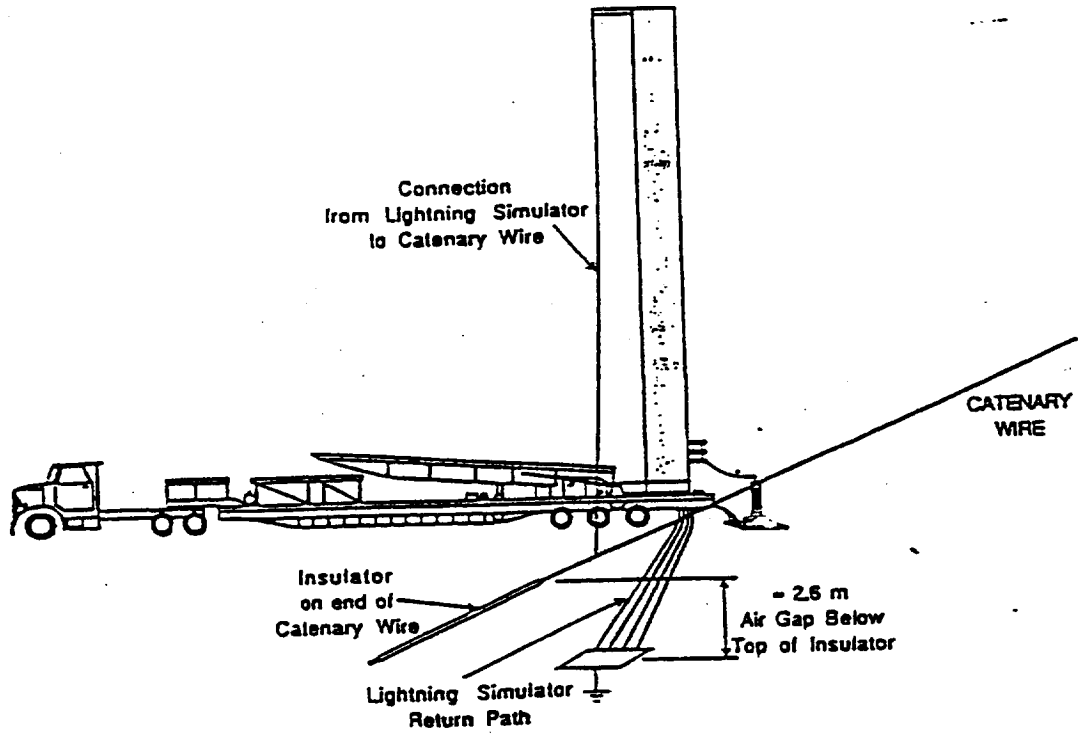

Figure 4.3 Simulator-Catenary Wire Configuration

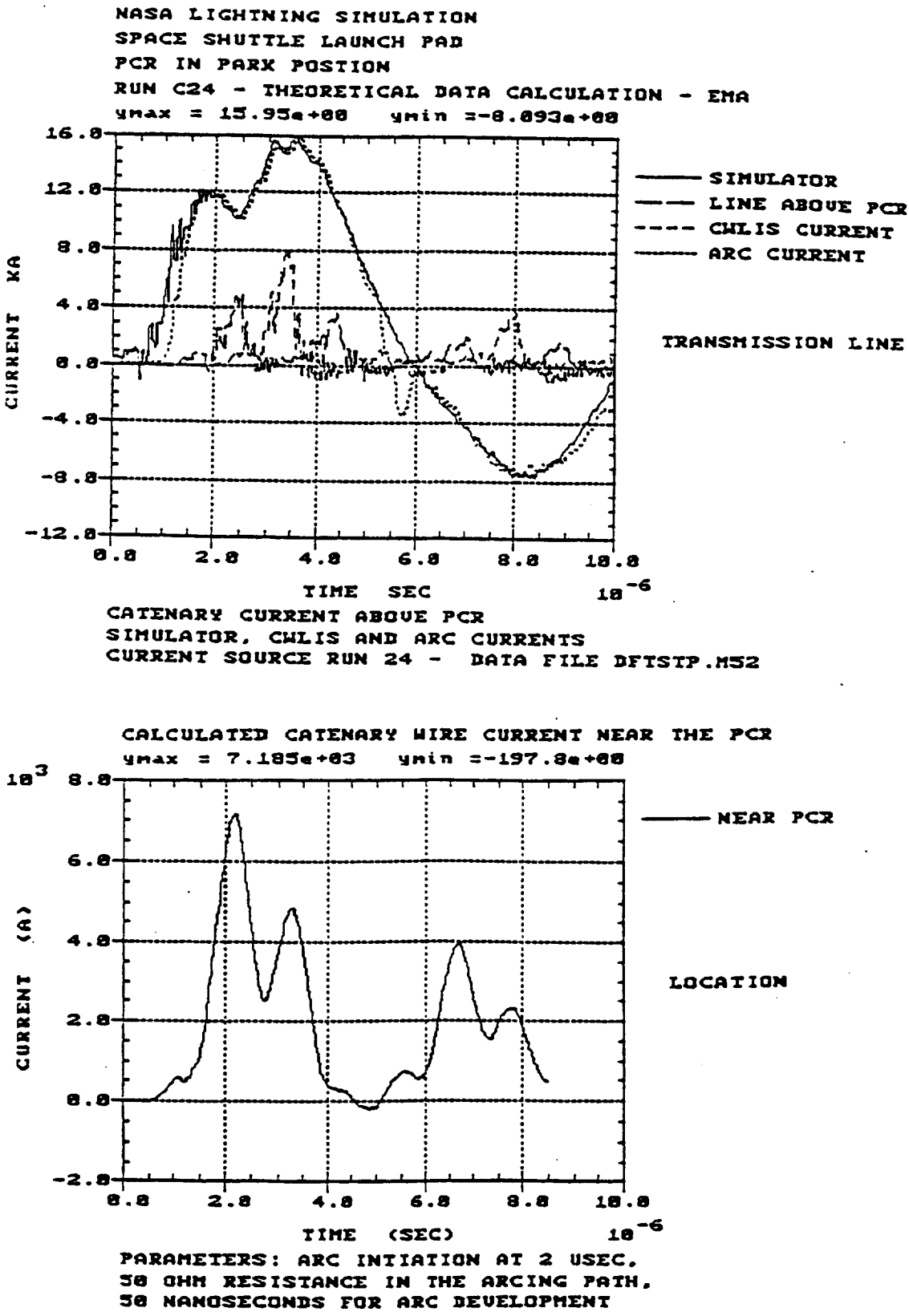

Figure 4.4 Calculated Catenary Wire Currents

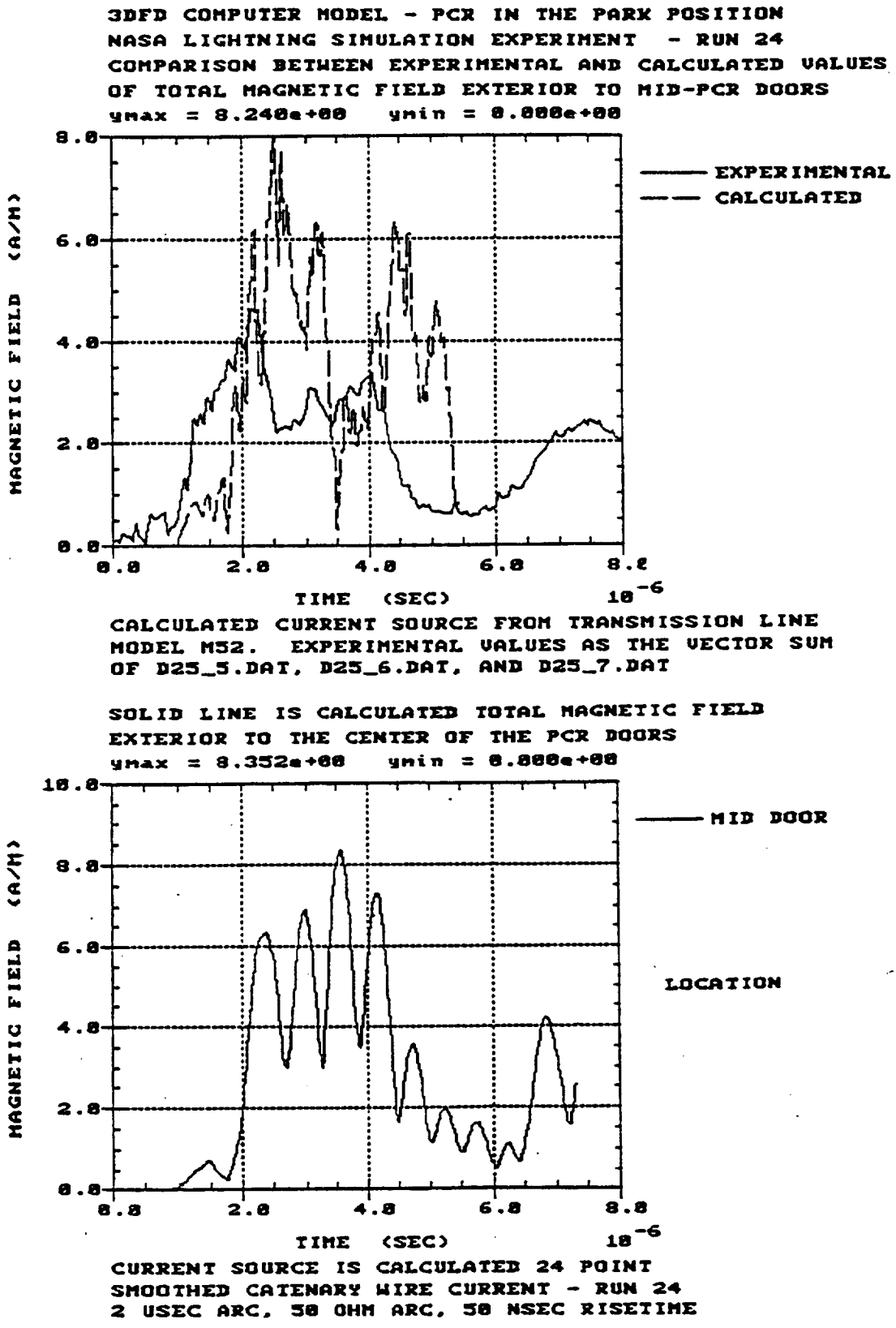

Figure 4.5 Total Magnetic Field Comparisons at the PCR Door Center

CHAPTER 5

DIRECT ATTACHMENT IN THE PARK POSITION

5.1 Simulation of the June 25, 1994 Lightning Strike

On June 25, 1994, a direct lightning attachment occurred to the Rotating Service Structure on Pad B. TV cameras show the attach point to be on the framework on the top outside corner nearest the back of the PCR. The geometrical relationships between the attach point, the RSS and the catenary wire is shown if Figure 5.1 [5]. A lightning detection system operated by CCAS Weather Operations indicated the peak amplitude of the strike to be within 16 to 20 KA [5]. No risetime or waveform measurements were available. Risetime statistics due to Leteinturier, et al. [9] [10], predict upper and lower bounds for the risetime of about 180 KA/usec and 18 KA/usec respectively as shown in Figure 5.2. These two risetimes were used to predict bounds for the system response for an 18 KA strike. Limiting waveforms corresponding to these bounds are shown in Figure 5.3. In particular, the finite difference methods of Chapters 2 and 3, using these input waveforms, were applied to this strike to obtain predictions of the coupling to the PCR interior due to direct lightning currents on the surface of the PCR.

In this case the Orbiter is absent, and the PCR and RSS are rotated back to the Park position; the PCR doors are closed. In this case the primary interest is in electric and magnetic fields which may propagate to the PCR interior, primarily through seams formed by insulating gaskets around the main doors. These seams are approximately 1.5 inches wide and are treated as apertures as described in Chapters 3 and 4. The five vertical seams 18 meters long are interrupted at 3-meter intervals by door hinges and buckles. The horizontal seams, at the top and bottom of the doors, are 11 meters long and are not interrupted by metal jumpers. The apertures are represented by equivalent polarizabilities Pe and Ph (with components calculated from equations 3.10 - 3.12), which multiply the time derivatives of the electric and magnetic fields at the exterior of the seam, and give equivalent electric and magnetic dipole current densities at the interior door seam locations. These interior dipoles are then used as source currents to drive a completely different 3DFD interior problem. The interior PCR grid in these calculations are .5 meter cubes and include elements of structure inside the PCR. The structure and locations of test points interior to the PCR are shown in Figure 5.4.

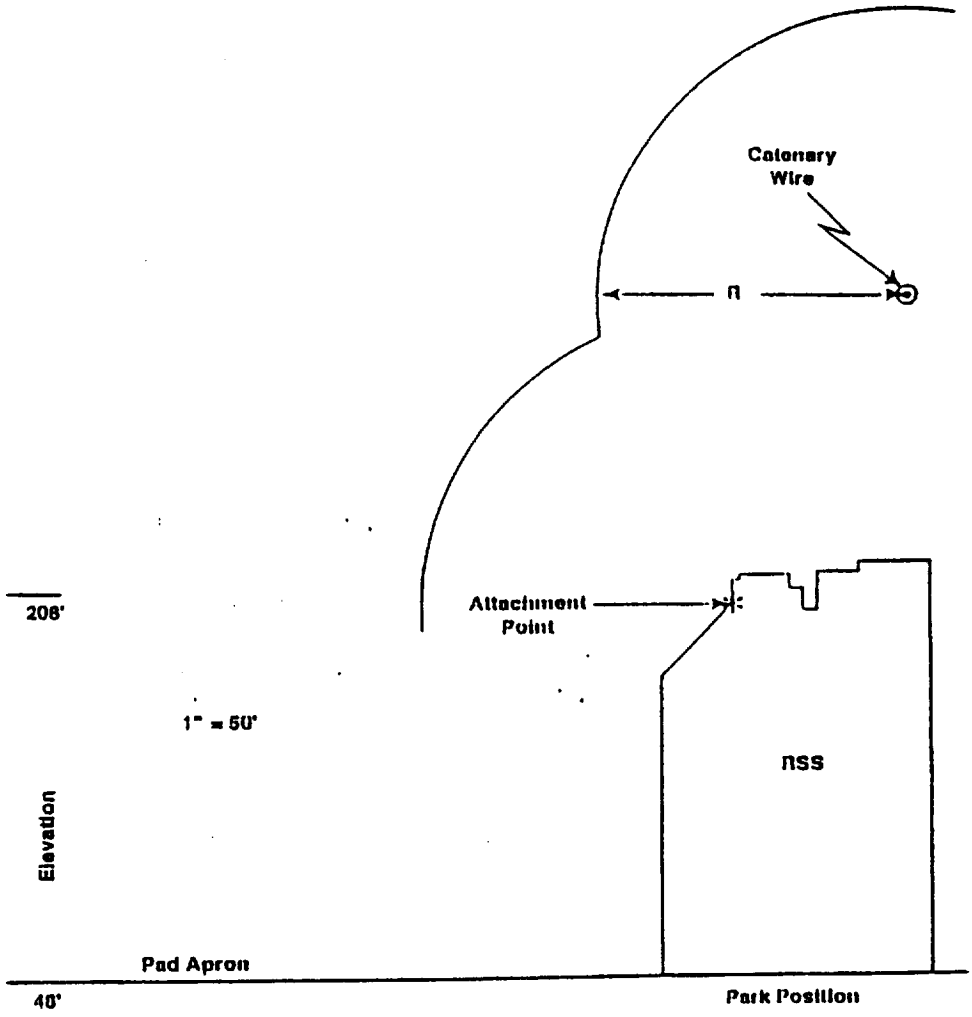

Figure 5.1 **The Relative Geometry of the RSS Frame, Catenary Cable and the Attachment Point of the June 25, 1994 Lightning Strike**

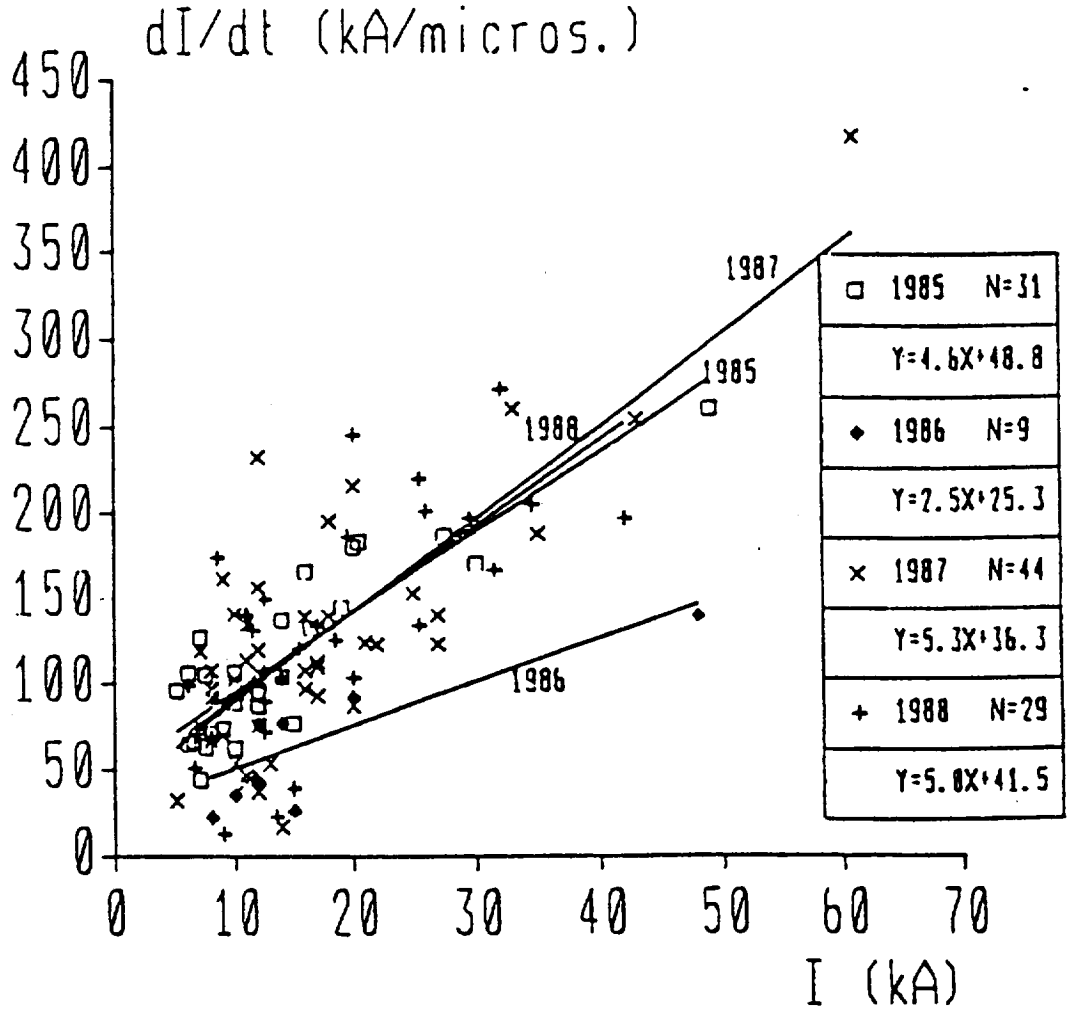

Fig. 6. Peak current derivative versus peak current. Linear fit equations and curves for 1985 to 1988 data.

Figure 5.2 Upper and Lower Bounds for the Initial Time Derivative of the June 25, 1994 Lightning Attachment taken at I = 18 KA

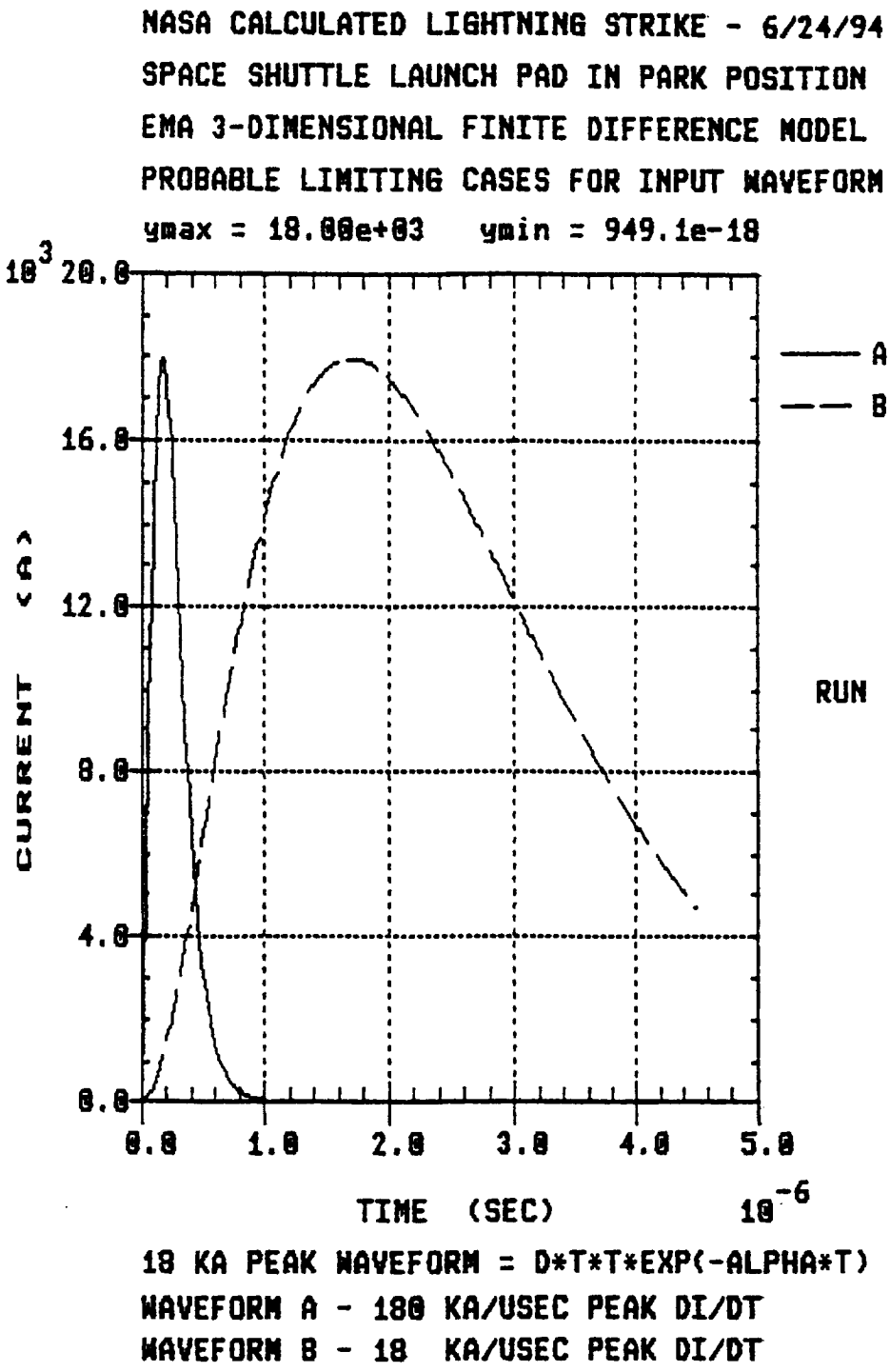

Figure 5.3 **Assumed Fast (A) and Slow (B) Risetime Waveforms Associated with the June 25, 1994 Lightning Attachment. The Time-Squared Multiplier Assures Zero Time Derivative at Zero Time.**

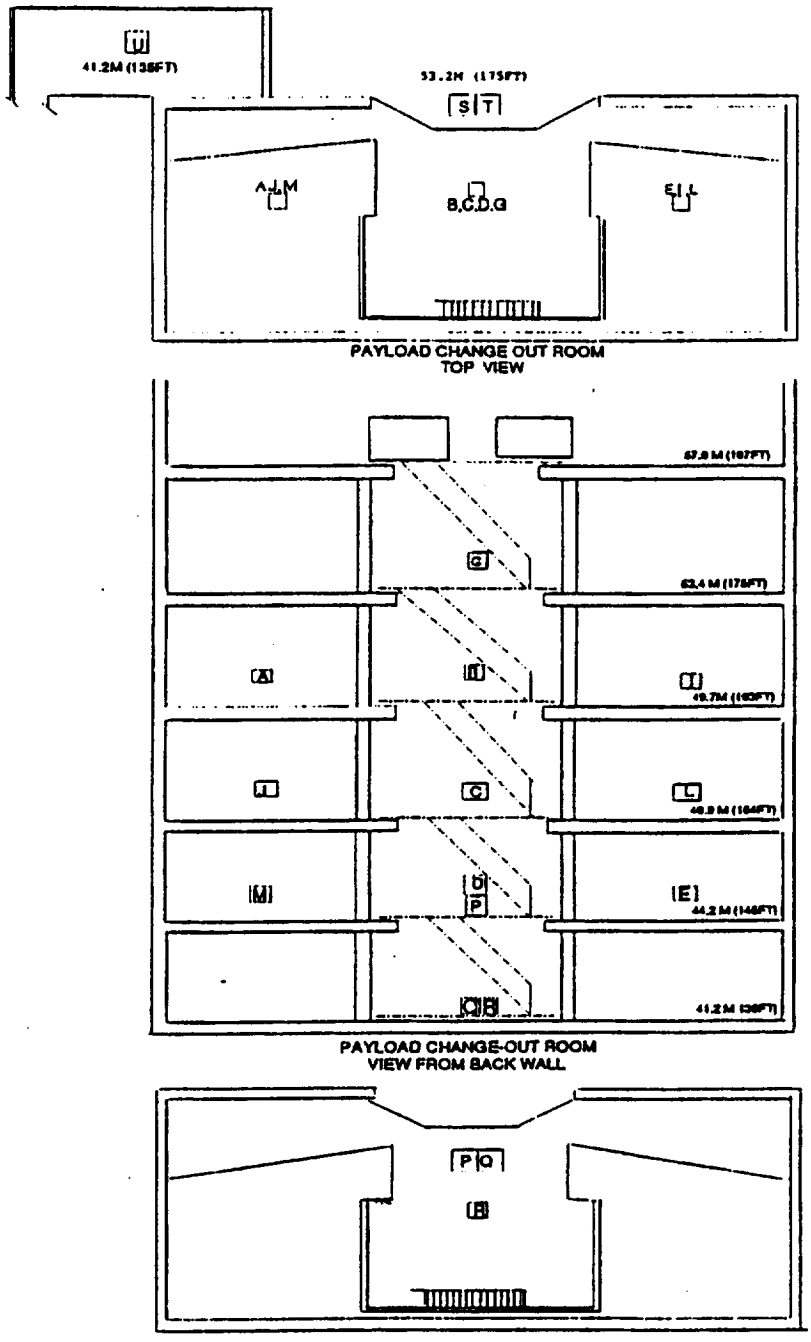

Figure 5.4 **Frontal and Plan Views of the PCR Interior Showing Internal Platforms and the Location of PCR Internal Test Points**

5.2 External Direct Currents Resulting from the June 25, 1994 Strike

It is also of interest to calculate some of the direct external currents due to the direct lightning attachment to the RSS. There are three points of contact of the RSS with the ground which provide the primary grounding points for the lightning charge. Two of these are at the wheel-track interface at the end of the two exterior legs of the RSS. The third is at the pivot point of the RSS. Figure 5.5 shows calculated currents in each of the legs and at the pivot point. For each quantity calculated there are two sets of curves corresponding to the limiting input waveforms A and B shown in Figure 5.3. In either case the current in each of the exterior legs is about 5 KA and about 3 KA at the pivot point. This accounts for 13 of the 18 KA input. The other 5 KA goes into the FSS. From the 5 KA current there was apparently some damage to controllers for the RSS wheel drive contained in metal cabinets box on the west leg.

5.3 External and Internal PCR Field Responses due to the June 25, 1994 Strike

Representative responses for the external electric and magnetic fields at the PCR door center are shown in Figures 5.6 and 5.7; the time derivatives of these fields are shown in Figures 5.8 and 5.9. In actuality, the time derivatives are obtained at each door seam location, thirty 3-meter vertical seam segments and two 11-meter horizontal seam segments. These locations drive the PCR interior through the field time derivatives according to the polarizability equations 3.6 through 3.12.

Some representative fields internal to the PCR shown in Figures 5.10-5.13. For illustrative purposes the responses are calculated independently for the vertical and horizontal door seams. The largest internal fields are due to magnetic field coupling to the horizontal door seams because the polarizability is proportional to the cube of the seam length. Here, it is inferred that coupling could be significantly reduced by using additional ground straps or grounding connections across horizontal seams. Also, it is seen again that higher frequency resonances corresponding to cavity resonance modes appear in the interior responses which could possibly couple to payload components. Resonance modes also appear in the external field responses as found also in the indirect coupling from the catenary wire. These resonances are coupled more strongly to the fast risetime waveform A, which has stronger spectral components which couple to some of the higher frequency resonance modes.

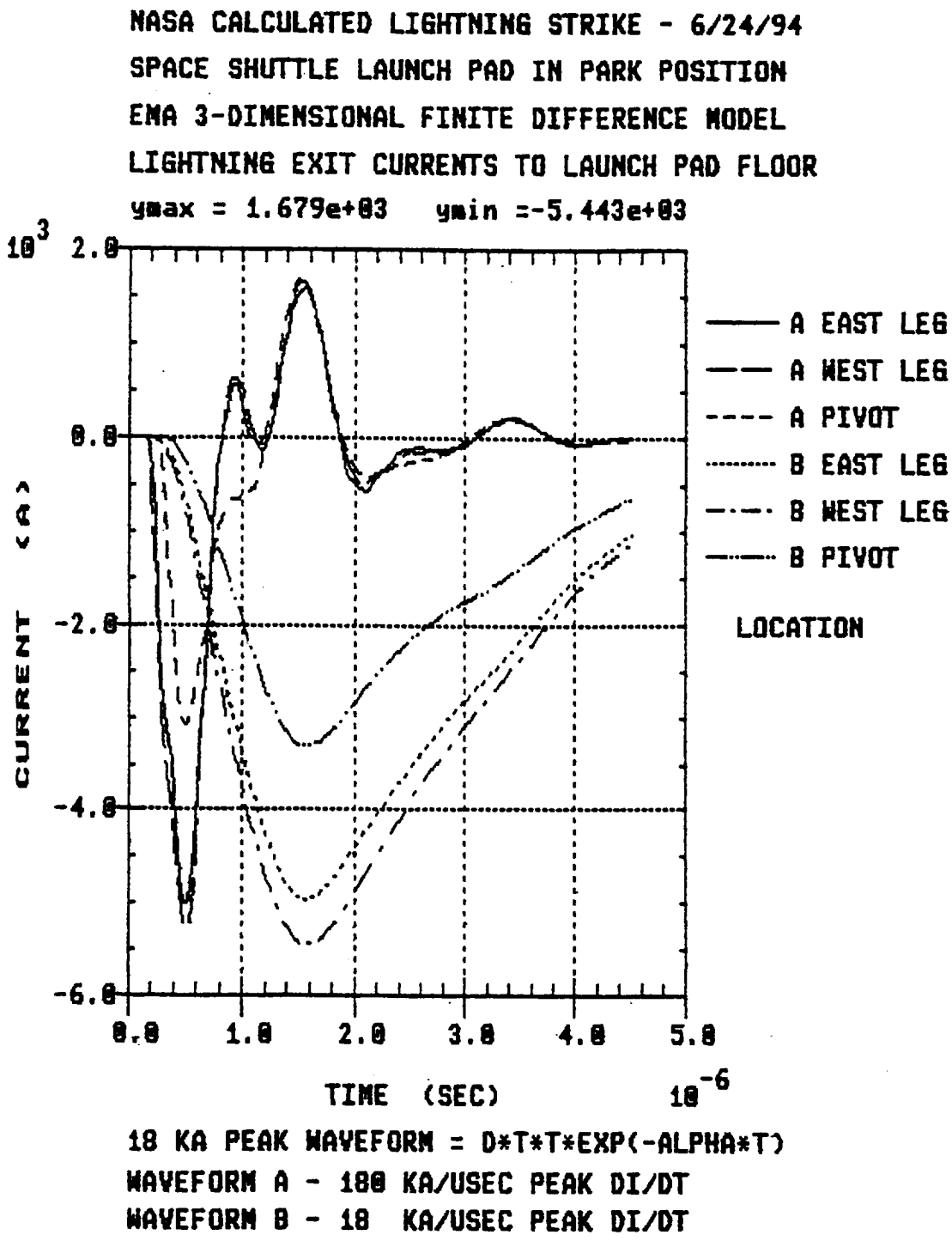

Figure 5.5 Direct Lightning Currents to Launch Pad Floor

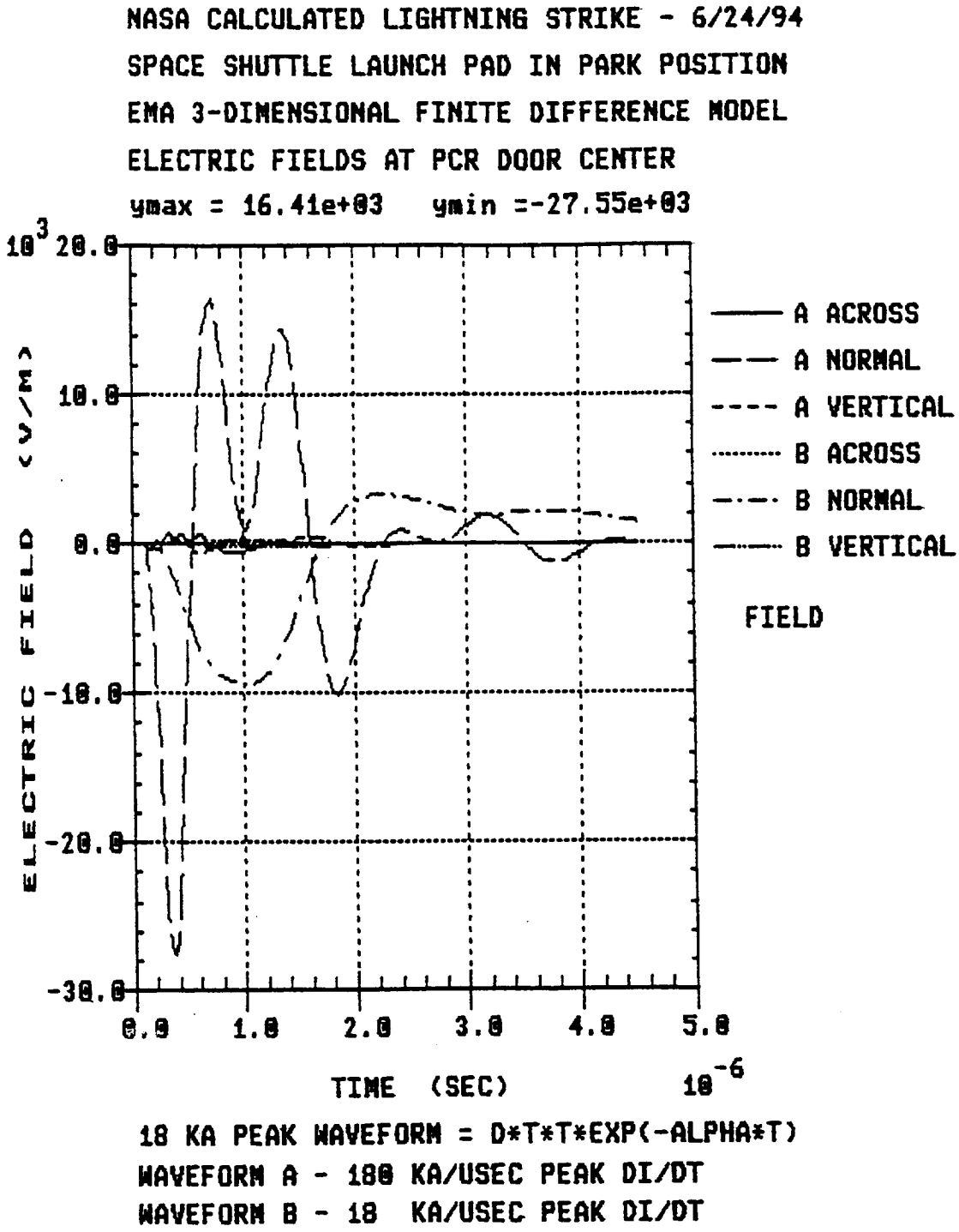

Figure 5.6 Electric Fields at PCR Door Center

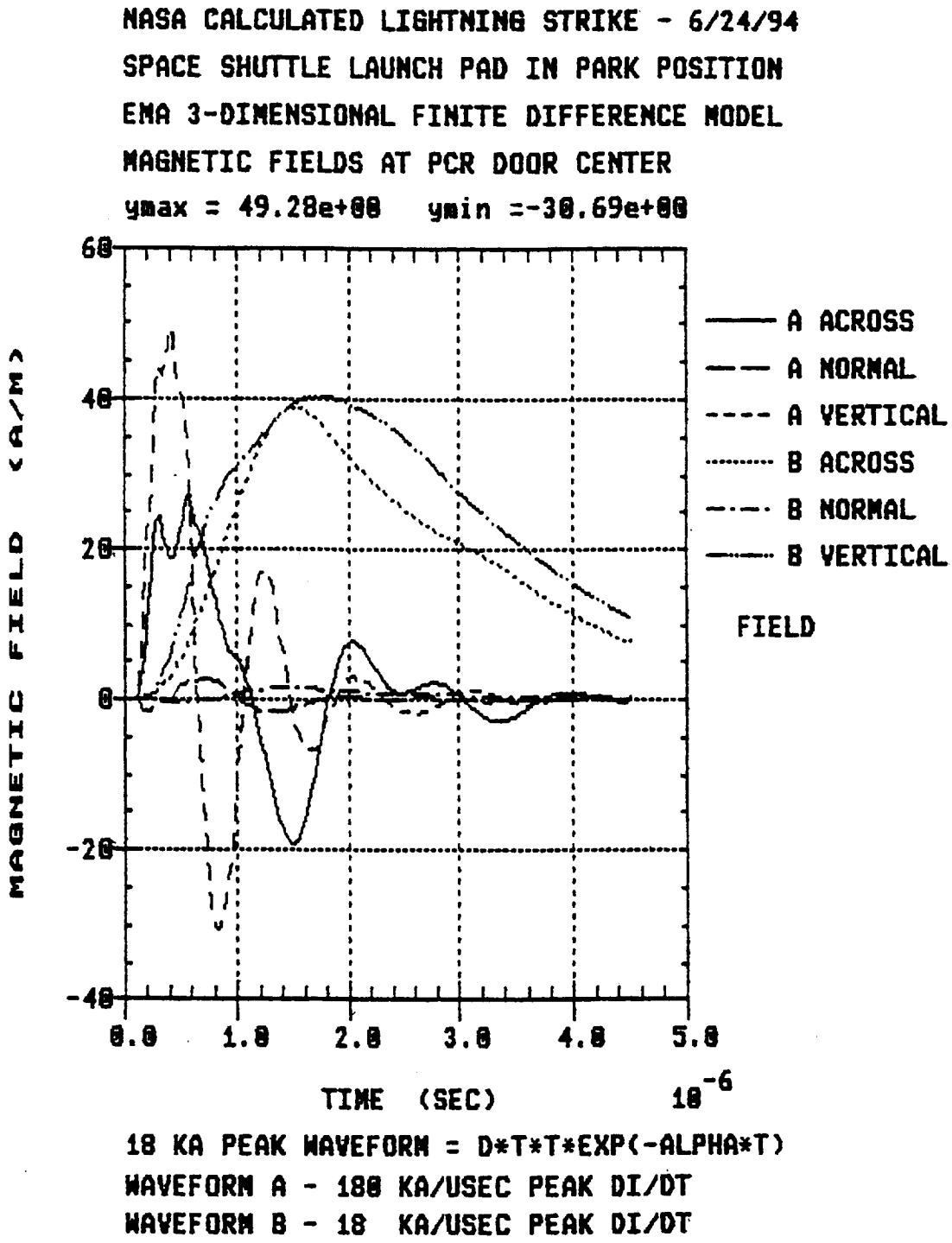

Figure 5.7 Magnetic Fields at PCR Door Center

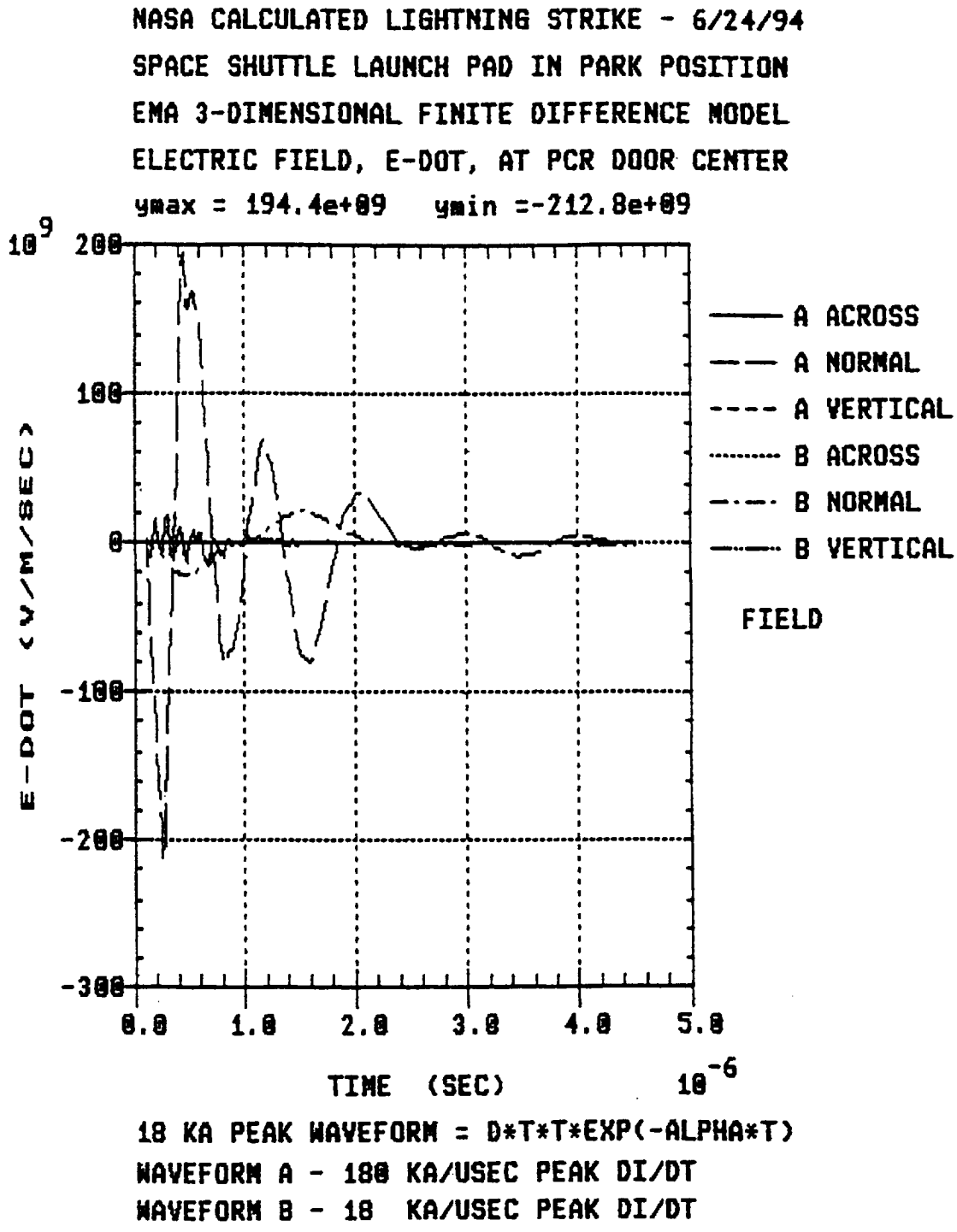

Figure 5.8 Electric Field, E-Dot, at PCR Door Center

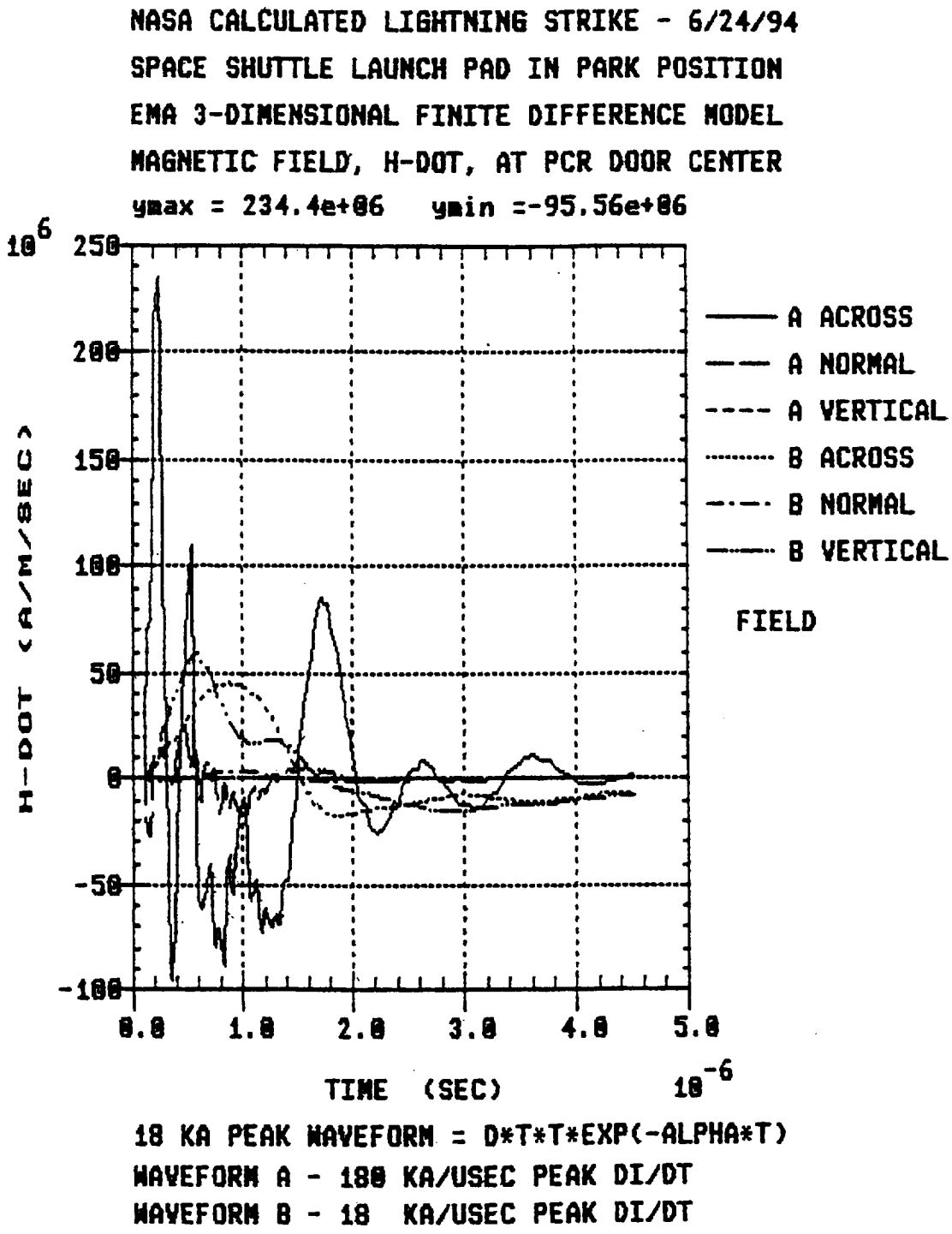

Figure 5.9 Magnetic Field, H-Dot, at PCR Door Center

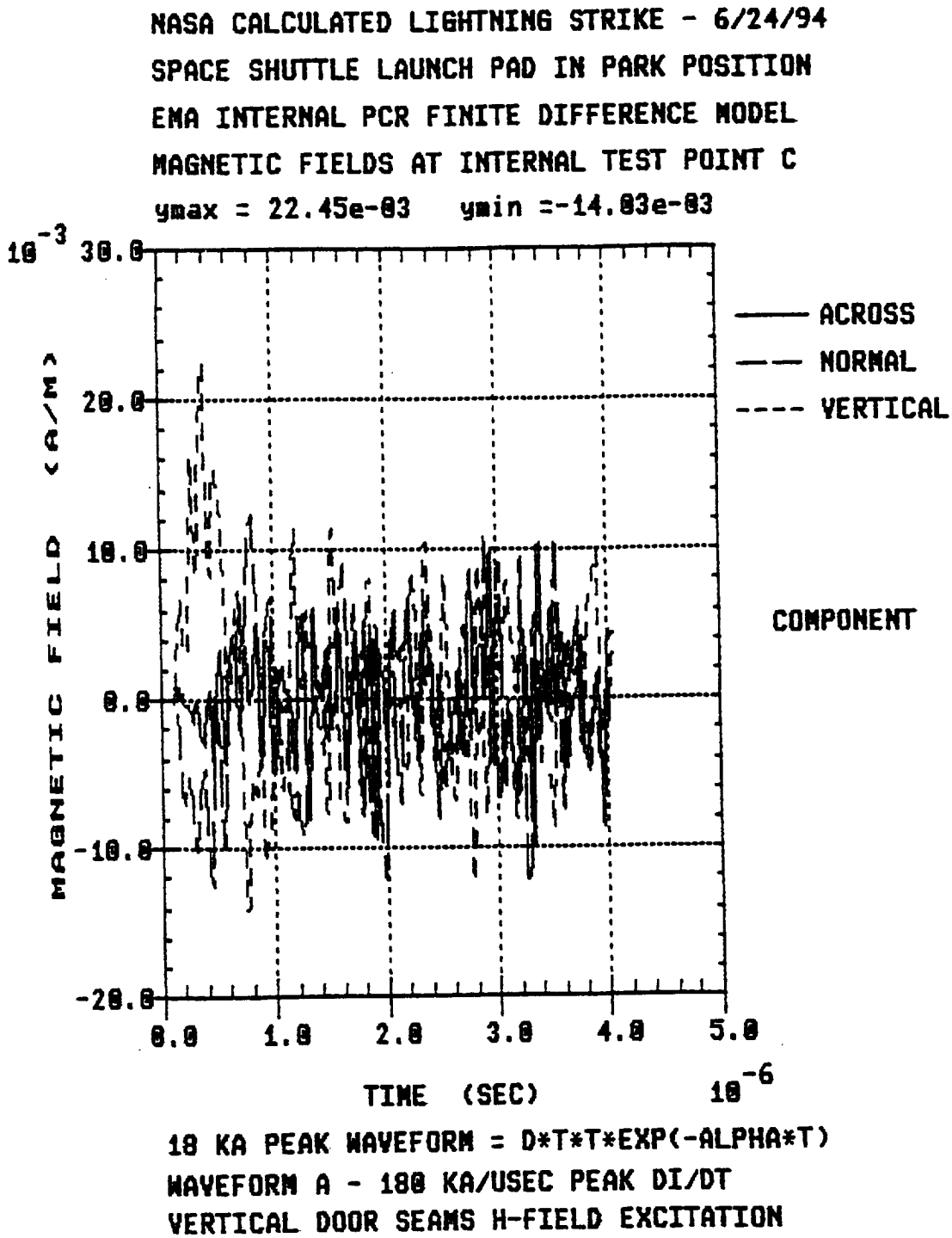

Figure 5.10 Magnetic Fields at Internal Test Point C; Vertical Door Seams H-Field Excitation

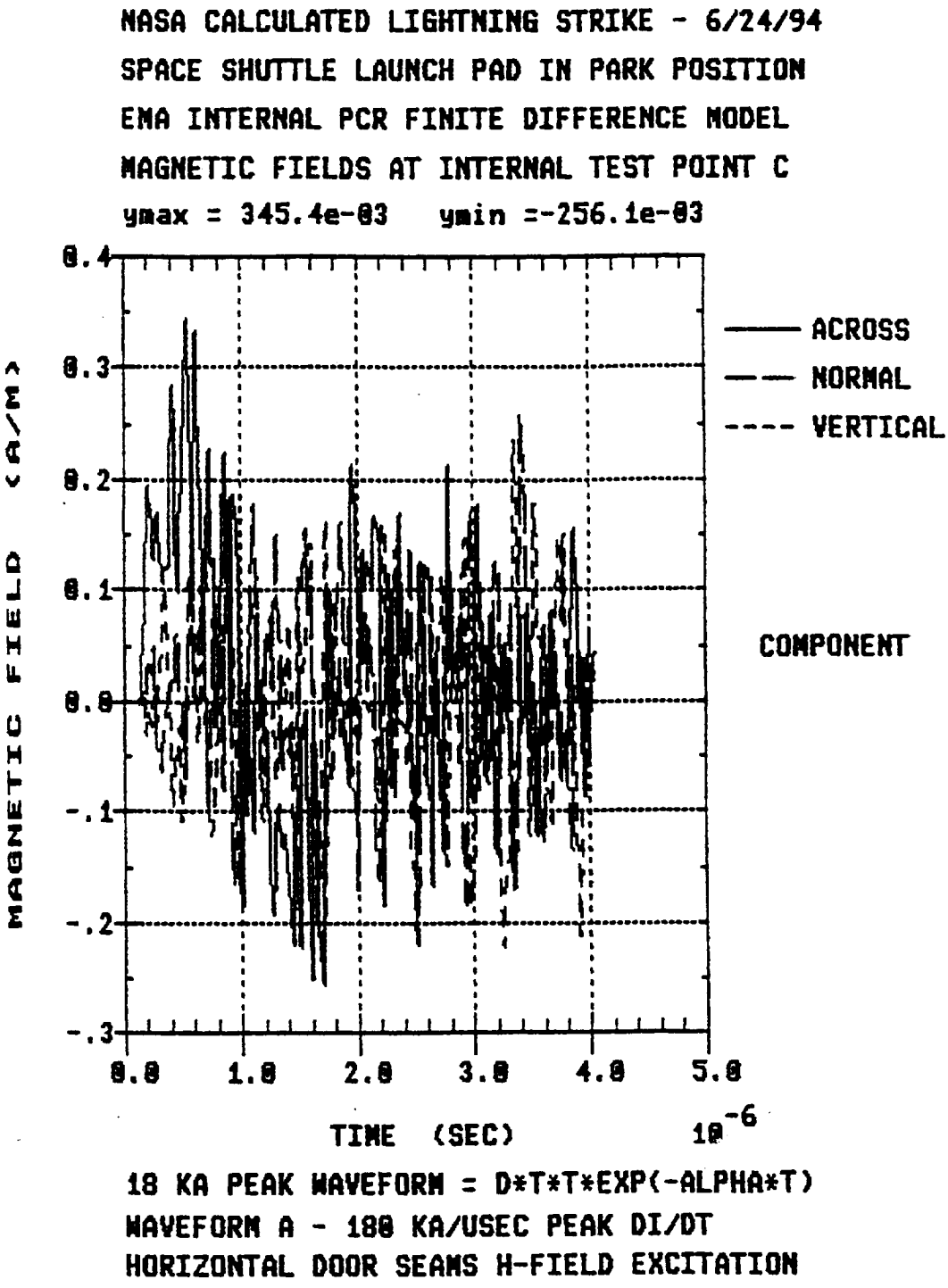

Figure 5.11 **Magnetic Fields at Internal Test Point C; Horizontal Door Seams H-Field Excitation**

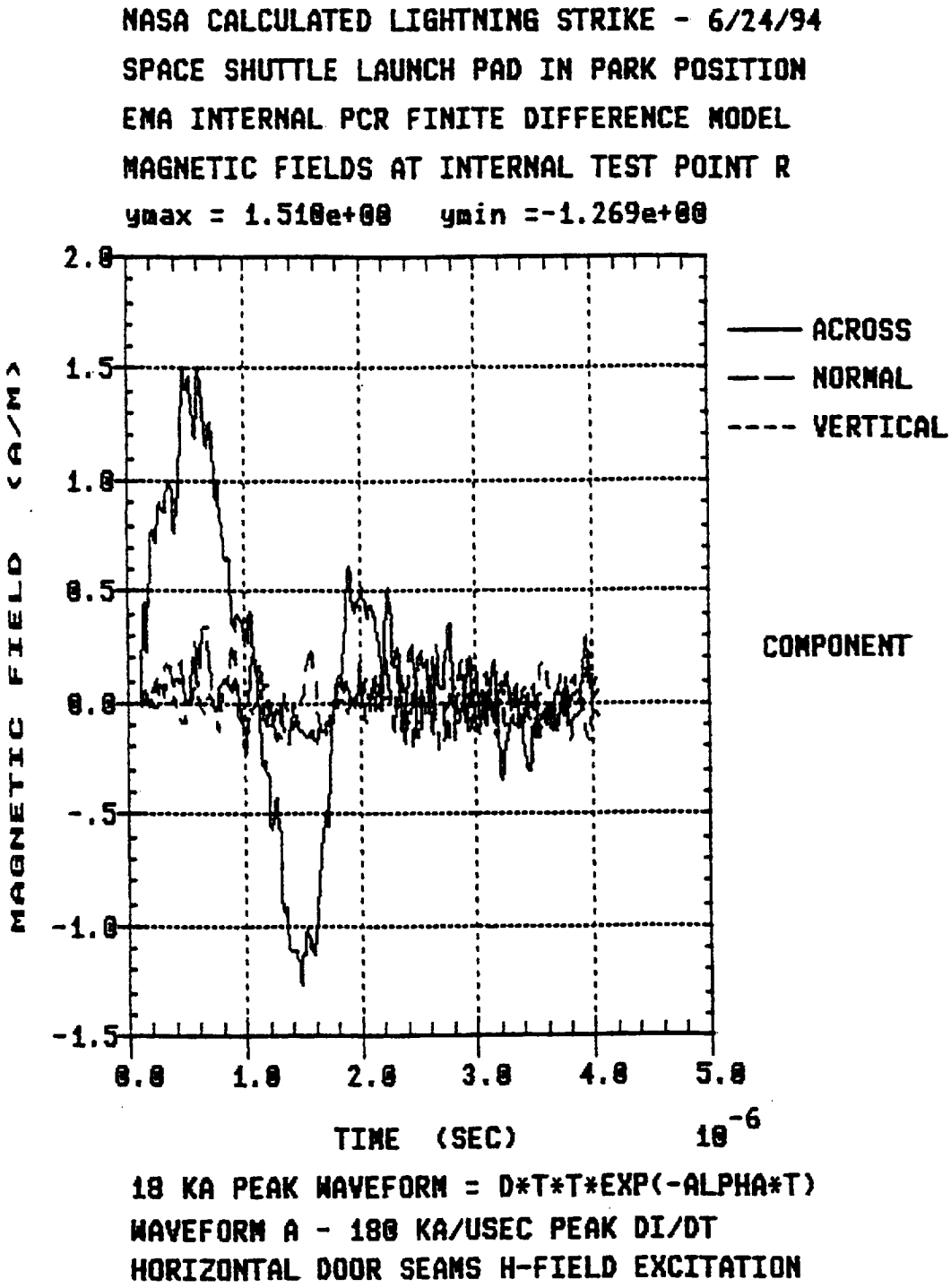

Figure 5.12 **Magnetic Fields at Internal Test Point R; Horizontal Door Seams H-Field Excitation**

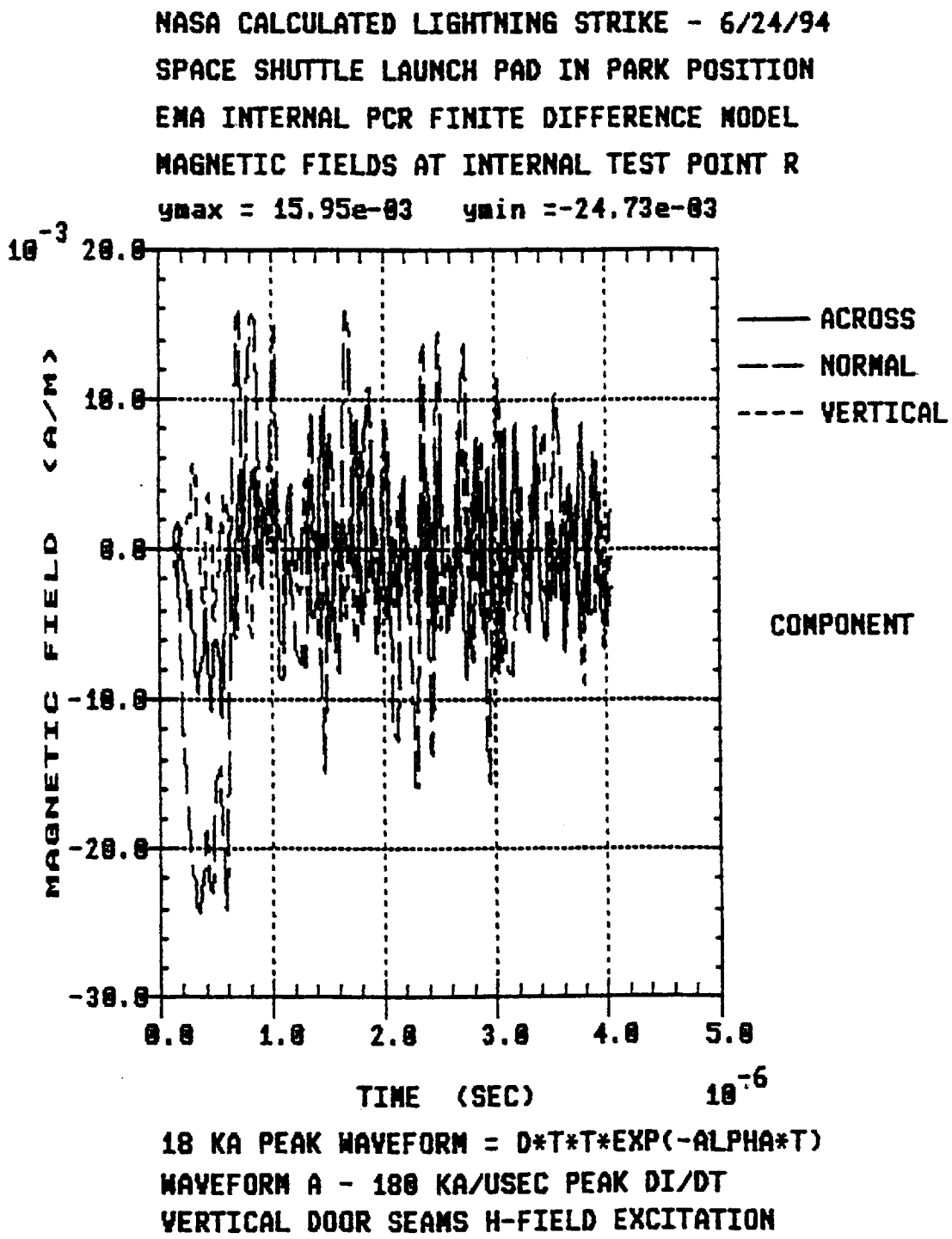

Figure 5.13 Magnetic Fields at Internal Test Point R; Vertical Door Seams H-Field Excitation

CHAPTER 6

PCR AND ORBITER IN THE MATE POSITION

6.1 The Mate Configuration

In the mate position, the PCR is rotated to mate with the Orbiter, the PCR and Orbiter payload bay doors are open and a payload is assumed being transferred from the PCR to the Orbiter. The external configuration is shown in Figure 6.1. The finite difference gridding is shown in Figure 6.2. A walkway is assumed extended from the Fixed Service Structure (FSS) to the Orbiter Cabin door. A White Room is at the interface between the walkway and the open cabin door. The response interior to the White Room will be discussed in Chapter 7.

A cut-away view of the PCR-Orbiter interface is shown in Figure 6.3. The primary lightning POE to the PCR interior is considered to be the inflatable seal between the PCR and the Orbiter representing an insulating gap approximately 9 inches wide. The Orbiter and PCR are connected by four ten-foot long ground straps located at the top and bottom of the Orbiter bay door hinges; and by one or two drag-on cables (which may or may not be connected) between the payload in the Orbiter bay and service equipment in the PCR interior. These wires and cables are modeled using the thin wire formalism described in Chapter 3.

Since this work was done it was determined that other apertures such as the gap between the Obiter and the open payload bay doors may also contribute significantly to the response interior to the PCR and the open payload bay. Therefore the results of this Chapter need to be considered as provisional, pending further calculations and possible additional experimental comparison with natural lightning data.

6.2 The Lightning Current Source – Strike to the Top of the Catenary Cable

The lightning current source, assumed for input, is a vertical lightning channel attached to the top of the catenary wire directly above the FSS. The lightning current waveform was assumed to be the NSTS Component A waveform [11] (See also Figure 6.4) with a 200 KA peak and a zero to peak risetime of 2 usec. The lightning current divides into two opposing directions at the top of the catenary. The resulting fields and currents at various locations are shown in Figures 6.5 to 6.10; a voltage waveform between the Orbiter and PCR is shown in Figure 6.8.

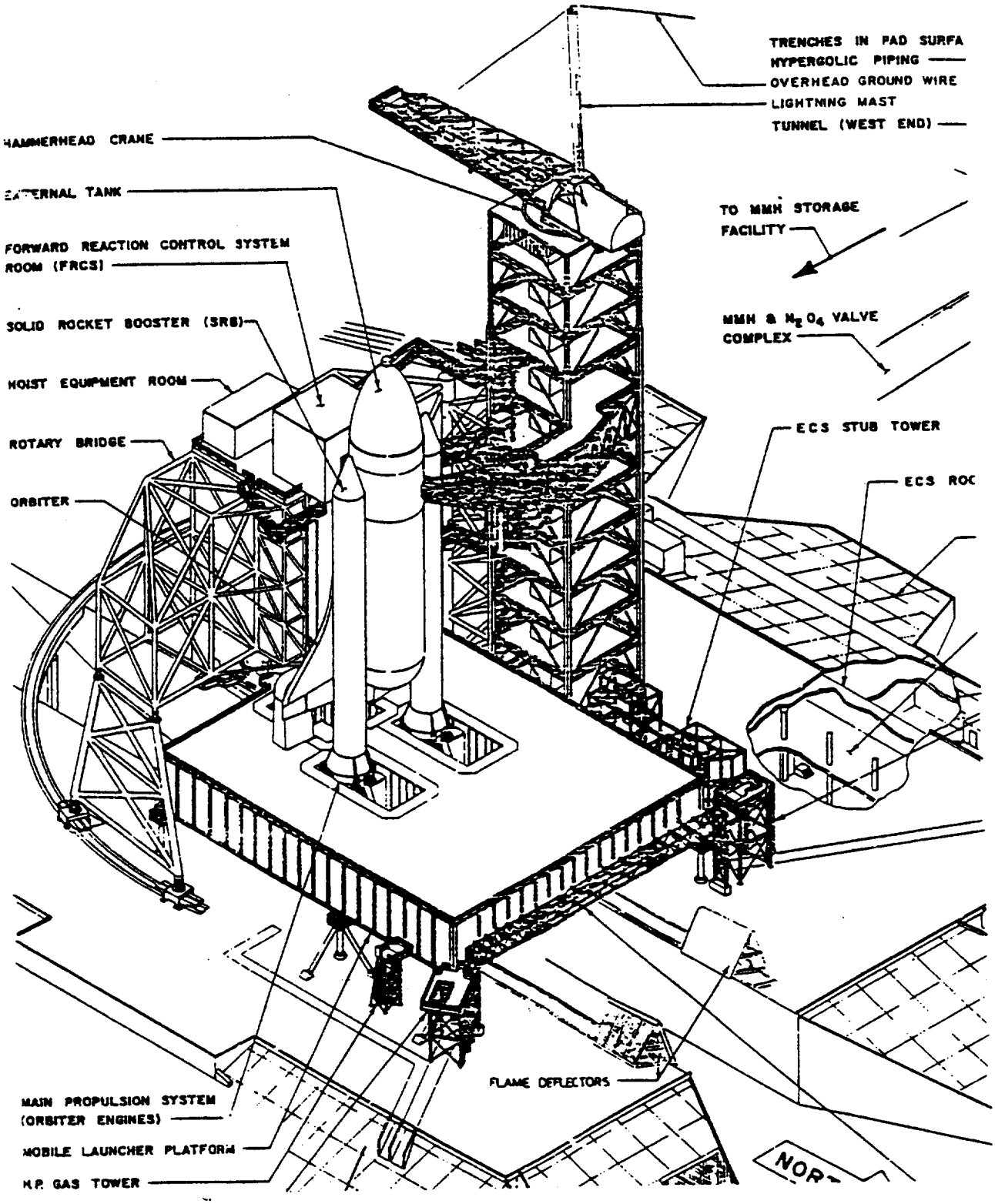

Figure 6.1 PCR and Orbiter in the Mate Position

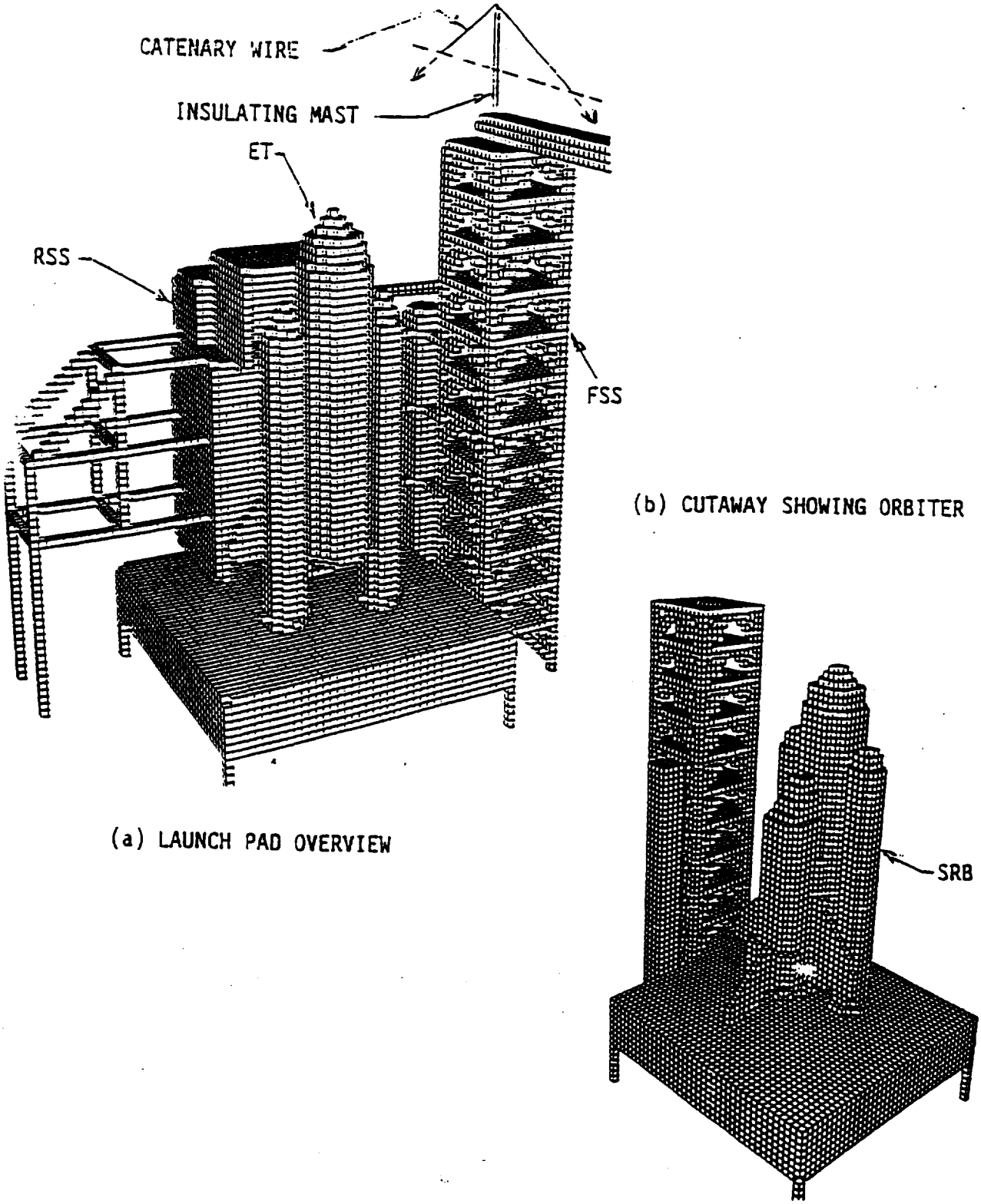

Figure 6.2 Finite Difference Gridding of the Mate Position

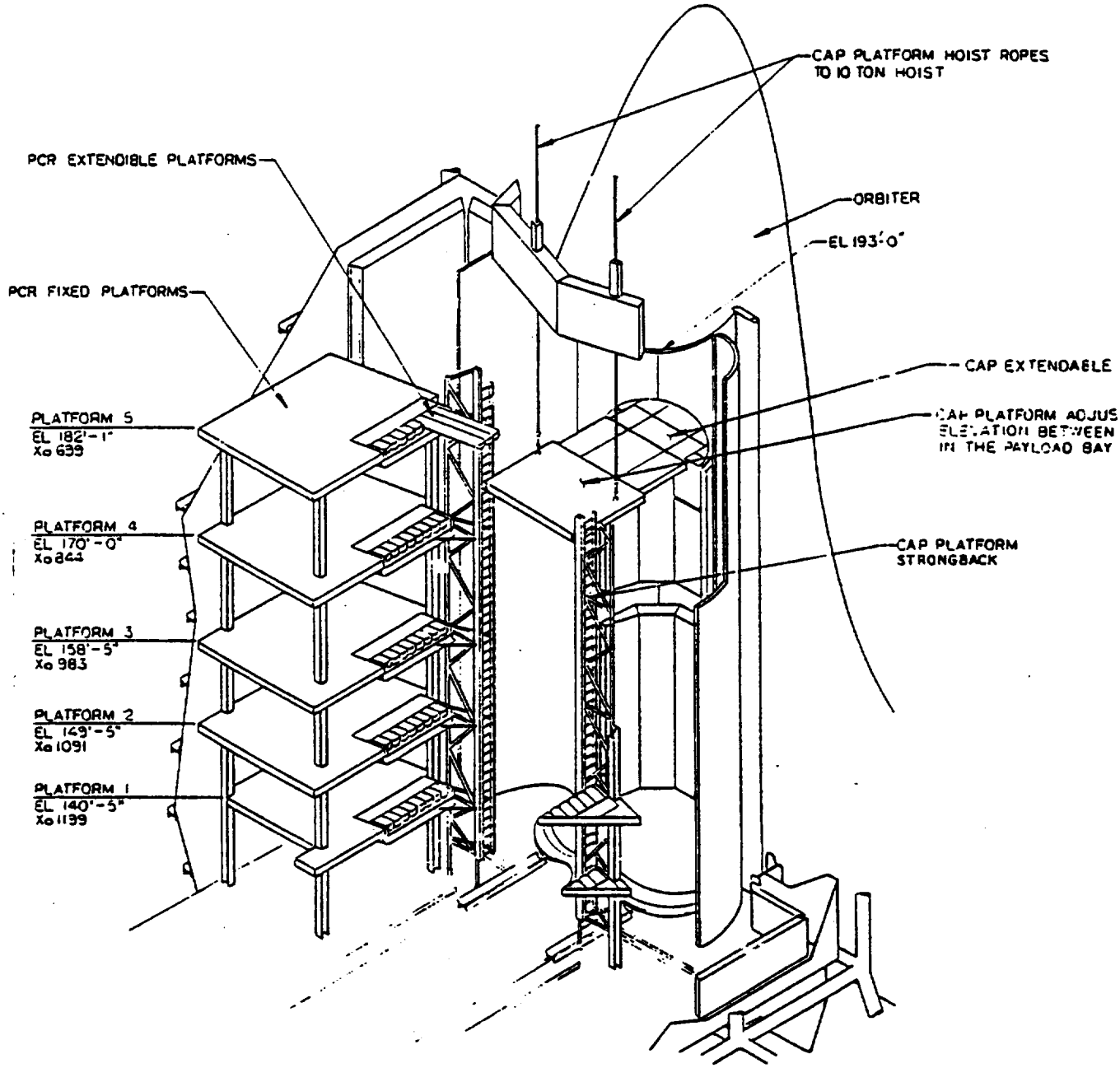

Figure 6.3 Interior Cut-Away View of PCR-Orbiter Interface

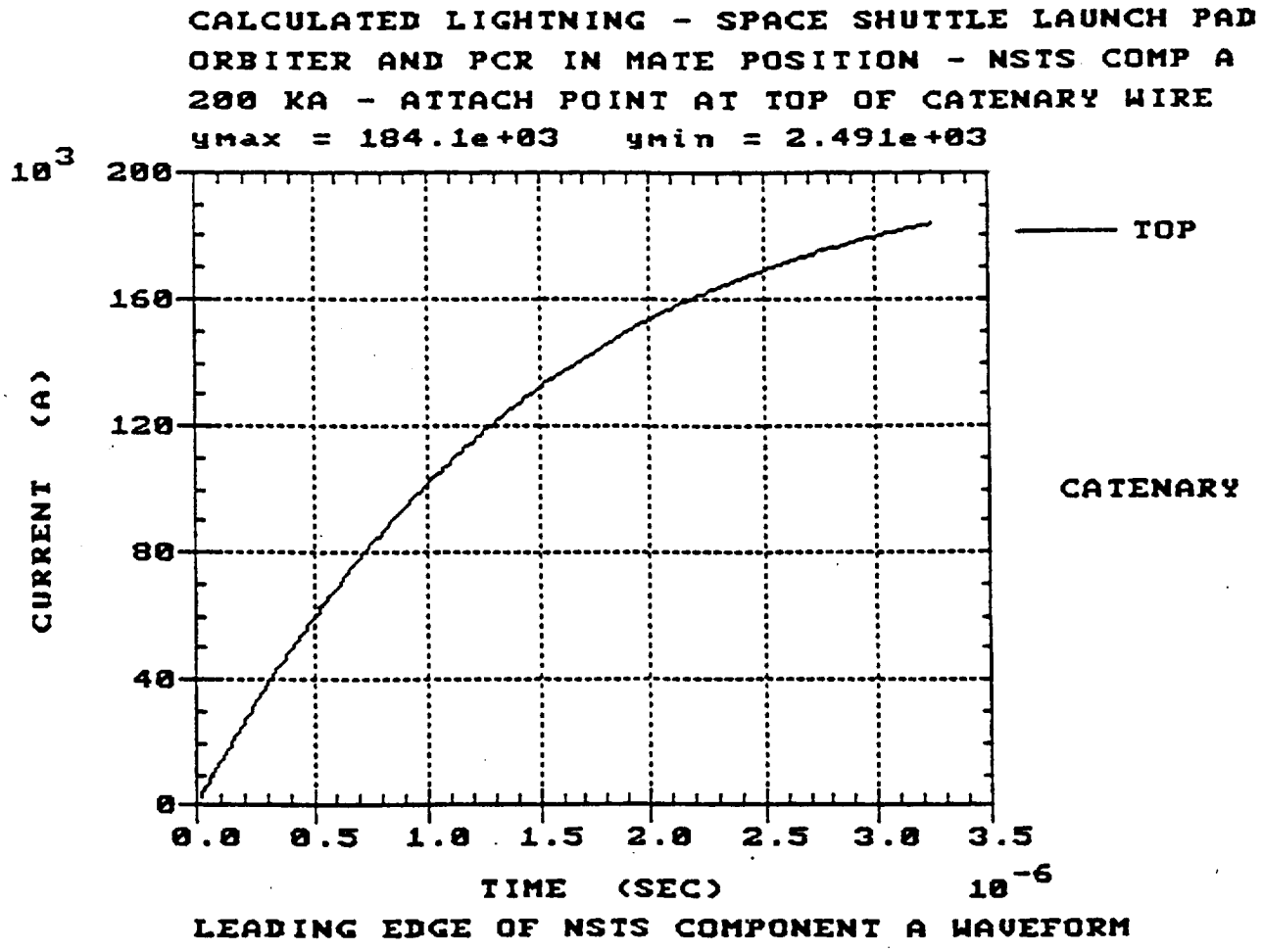

Figure 6.4 NSTS Component A Waveform

These results are expected to change with the location of the lightning attach point as well as changes in the lightning amplitude and waveform.

6.3 Electromagnetic Field, Current and Voltage Responses

The primary results may be summarized as follows for a strike simulated by the NSTS 07636 Component A lightning waveform [11] (See also Figure 6.4) to the top of the lightning protection mast:

1. The peak external magnetic field is about 200 A/m on top of the PCR, and on the order of 100 A/m or less, depending on position, near the PCR doors (Figure 6.5). The tangential field on top of the PCR closely follows the lightning input waveform.

2. The vertical magnetic field at the Orbiter-PCR gap varies greatly with position around the gap, both in sign and magnitude, and also in waveform (Figure 6.6). It is essentially the measurement (or indication) of the local surface current density. These fields are on the order of 60 A/m or less which also appears to be reasonable. The exterior magnetic field components near the long vertical gap are also shown in Figure 6.5.

3. The peak internal magnetic fields vary greatly with position inside the PCR ranging from about 10 A/m at a midpoint location (Figure 6.7) between the Orbiter payload and the interior PCR Service structure increasing to the gap values of the magnetic field for locations which approach the gap fields of about 60 A/m. The interior field has only a weakly oscillating component.

4. The voltage across the gap has a strong oscillating component. The voltage magnitudes are on the order of 10 KV at the peaks and a few KV at longer times (Figure 6.8). The magnitude is dependent on the risetime of the lightning current waveform.

5. The currents on the ground straps and drag-on cable have a strongly oscillating component, reflecting the gap voltage behavior, and have peak amplitudes on the order of a few 100 amps (Figure 6.9). The only effect of disconnecting the drag-on

cable is to slightly increase the ground strap currents. The currents appear to be roughly shared between the ground straps and the drag-on cable.

The source and nature of the oscillating components of the fields and cable currents need to be understood in more detail. This is expected to result from a spectral analysis of the numerical data which is discussed in Chapter 8. Also, the results seem to be very dependent on the length, number, and location of the ground straps connecting the Orbiter with the PCR – this dependence should be further investigated. Also it should be noted that the strike to the top of the lightning protection mast may not be a "worst case" scenario for coupling to the PCR interior. This is because the lightning current splits into two opposite directions at the top of the mast – thus canceling some of the generated magnetic field components on a plane perpendicular to and bisecting the catenary wire, which is in the neighborhood of the PCR location. It may be worth an additional computer run or two to investigate strikes to other locations on the catenary wire.

Also, finally, it may be very worthwhile to develop a frequency dependent transfer function between the catenary wire currents and the field and current responses at critical locations and elements of the Orbiter-PCR interface. If such a transfer function can be shown to be reliable, then responses at critical locations may be obtained from the transfer functions for any given lightning strike waveform – including any data from natural lightning events. In this connection, the data taken at the top of the PCR using the large loop antennas may be very useful in evaluating the transfer function development – as well as the other passive measurements in the PCR interior during natural lightning events.

In Figure 6.10, a schematic shows peak magnetic fields at selected locations inside the payload bay calculated by the finite difference model for the PCR in the mate position with the Orbiter; the response is due to a NSTS Component A simulated lightning attachment to the top of the catenary cable; the doors of the Orbiter are open in the interior of the PCR; in this case there are no drag-on cables connecting the Payload with the PCR interior; the other 4 ground straps are in place.

A "dummy" payload is simulated as a cylinder filling about 2/3 of the aft interior space of the payload bay. The points selected for data A, B, D, and E lie on a vertical line which lies just outside the payload cylinder toward the interior of the PCR. The point C lies in the middle of the empty portion of the payload bay.

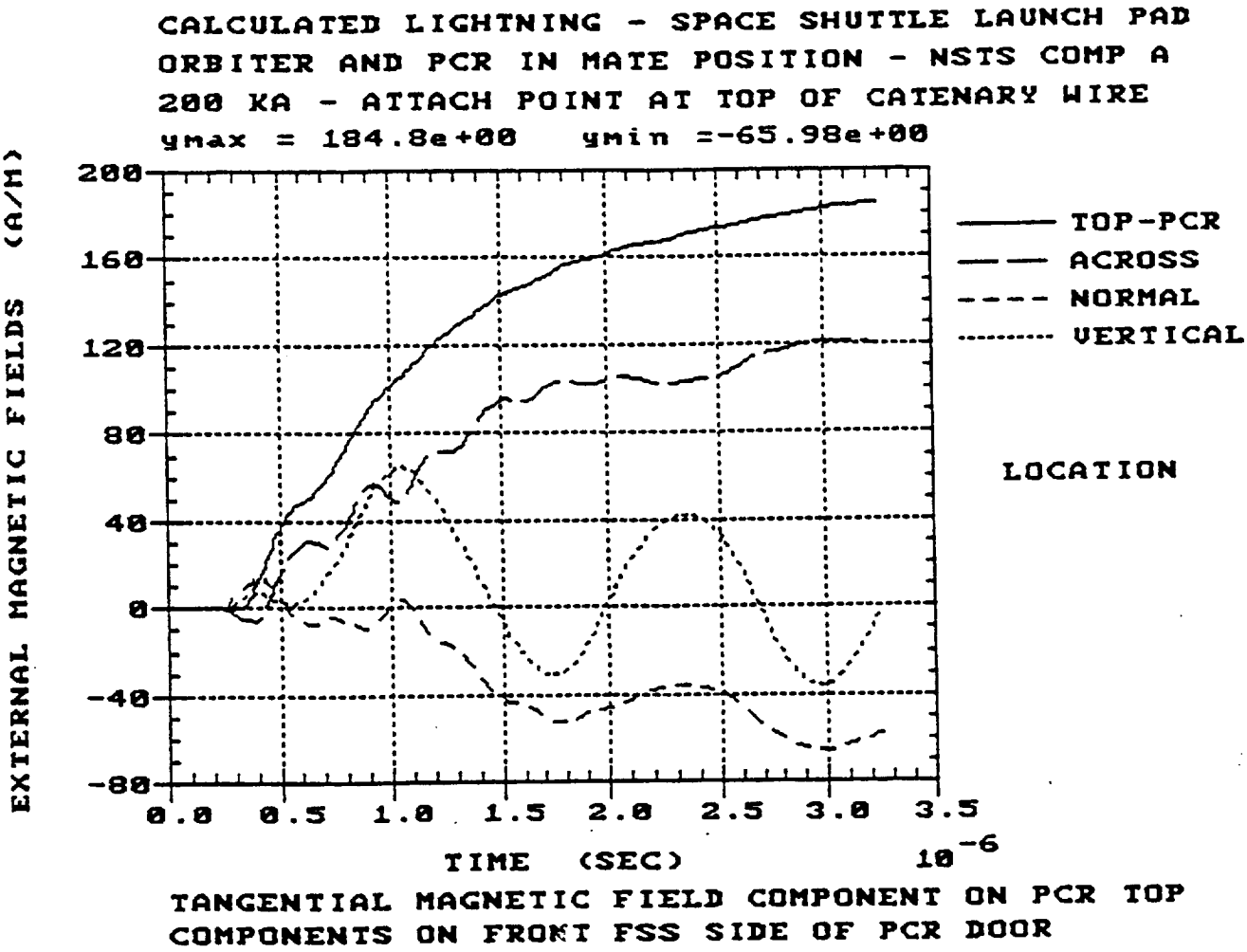

Figure 6.5 Exterior Magnetic Field Responses

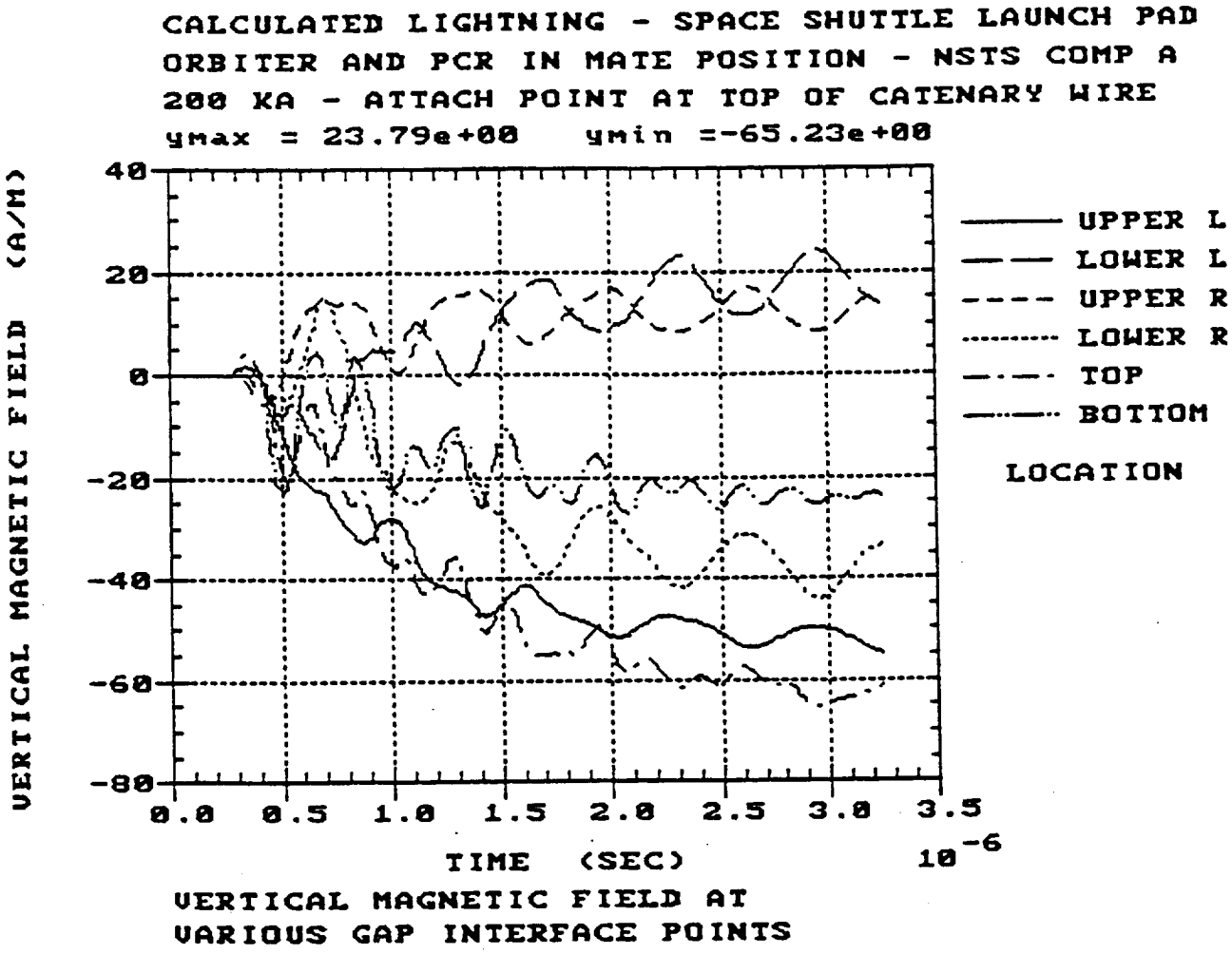

Figure 6.6 Vertical Magnetic Fields at Various Locations in the Gap Between the Orbiter and the PCR

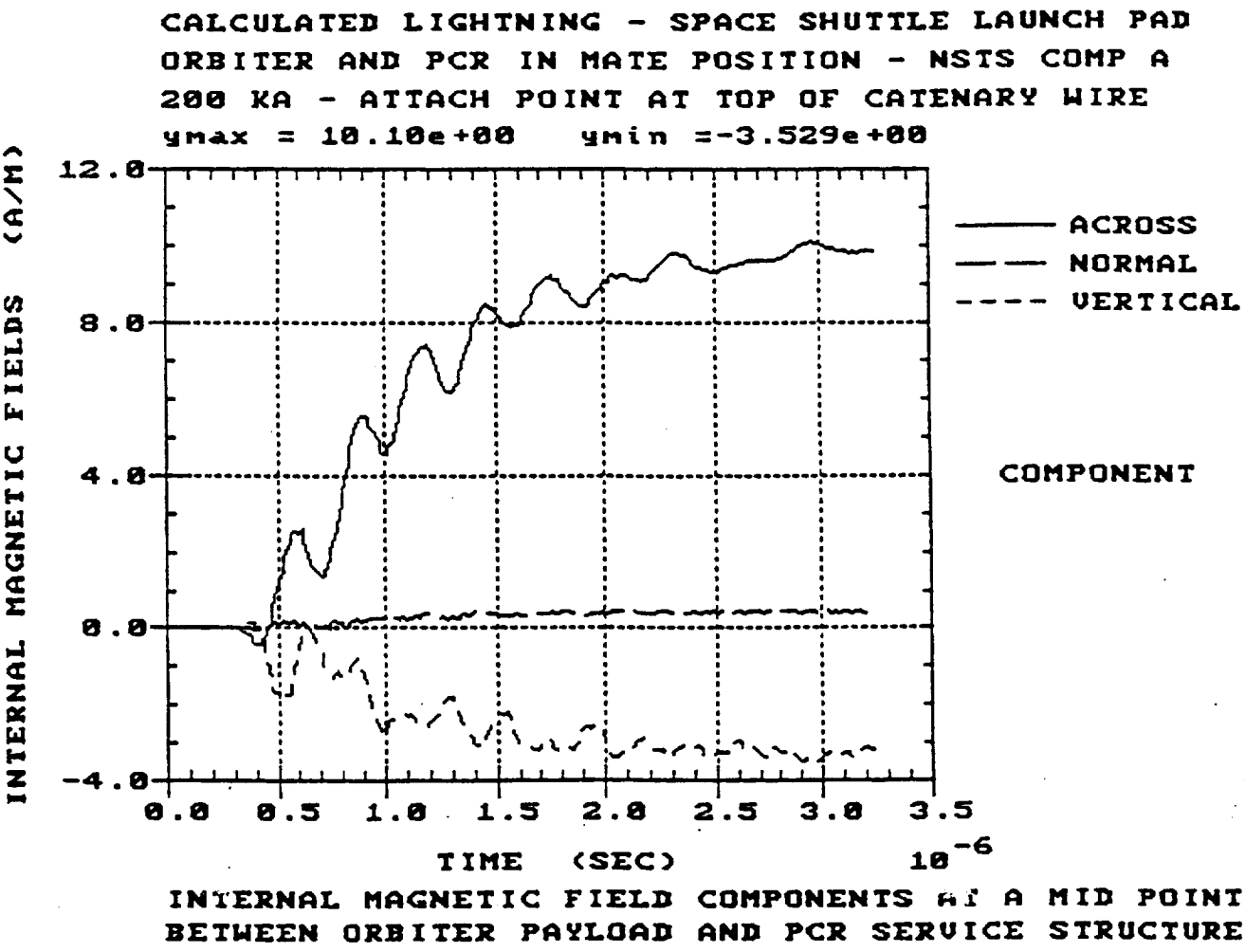

Figure 6.7 Interior Magnetic Field Responses

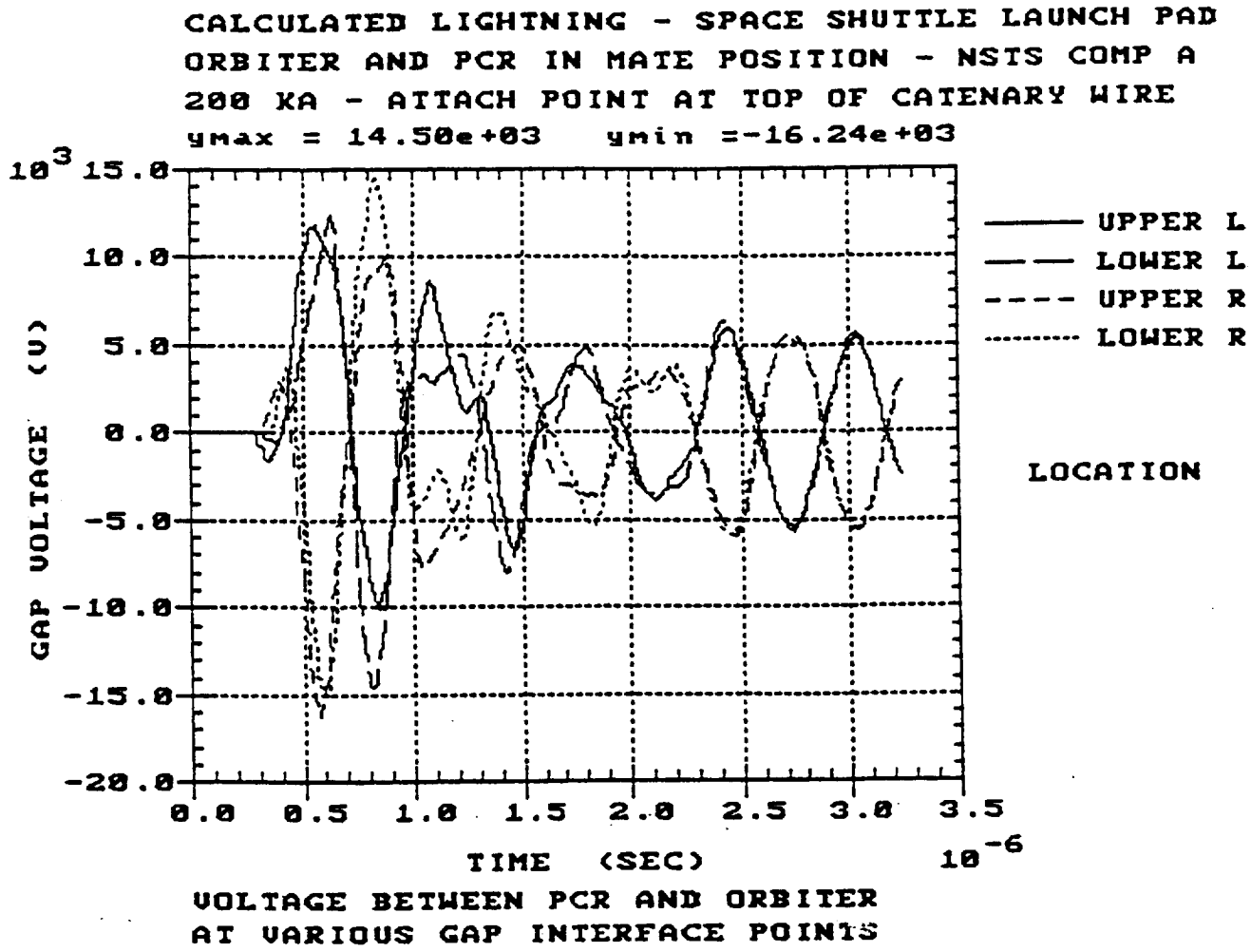

Figure 6.8 Voltage Between the PCR and Orbiter at Various Gap Interface Points

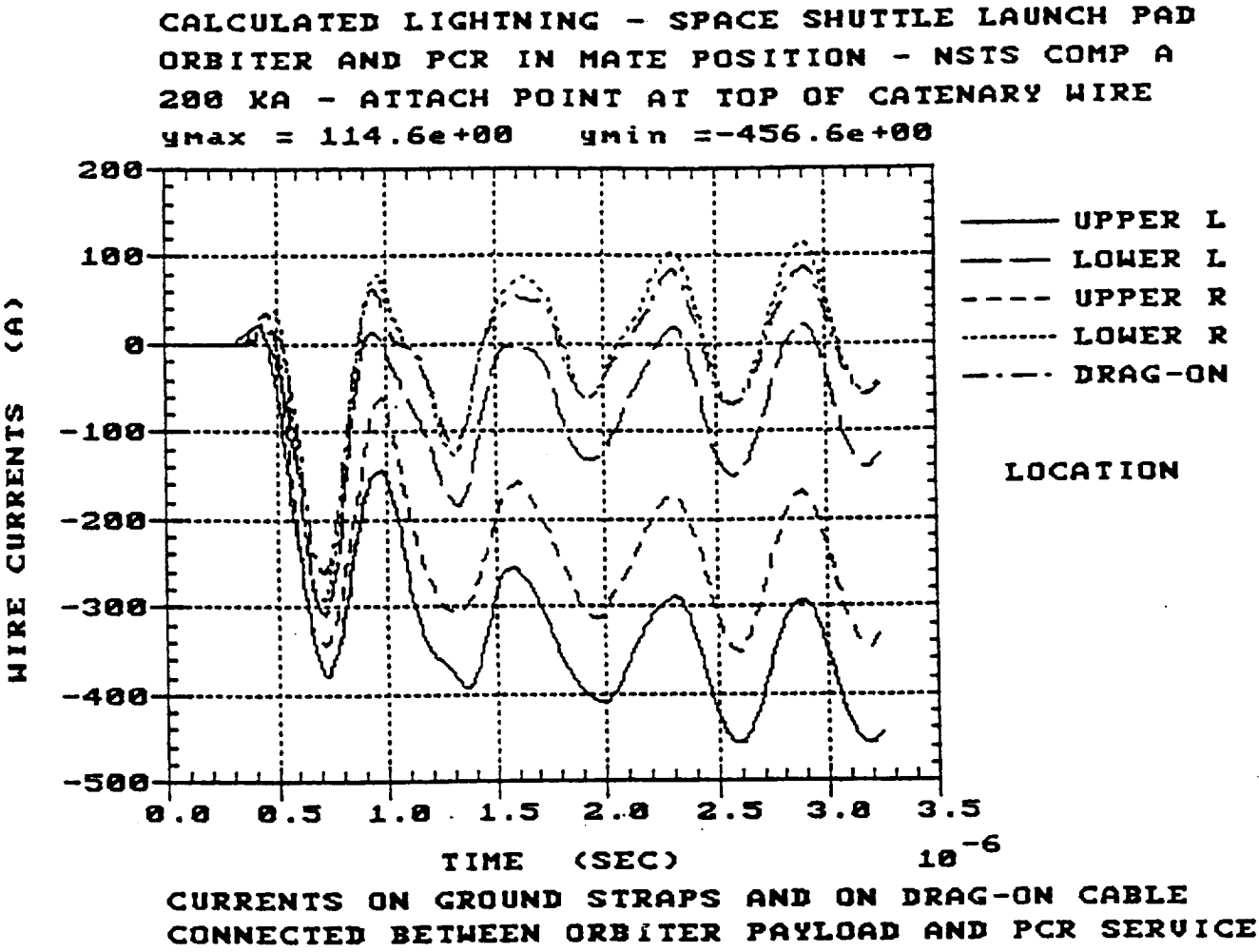

Figure 6.9 Currents on Ground Straps and Drag-On Cable

PEAK MAGNETIC FIELDS NEAR PAYLOAD AND IN PAYLOAD BAY

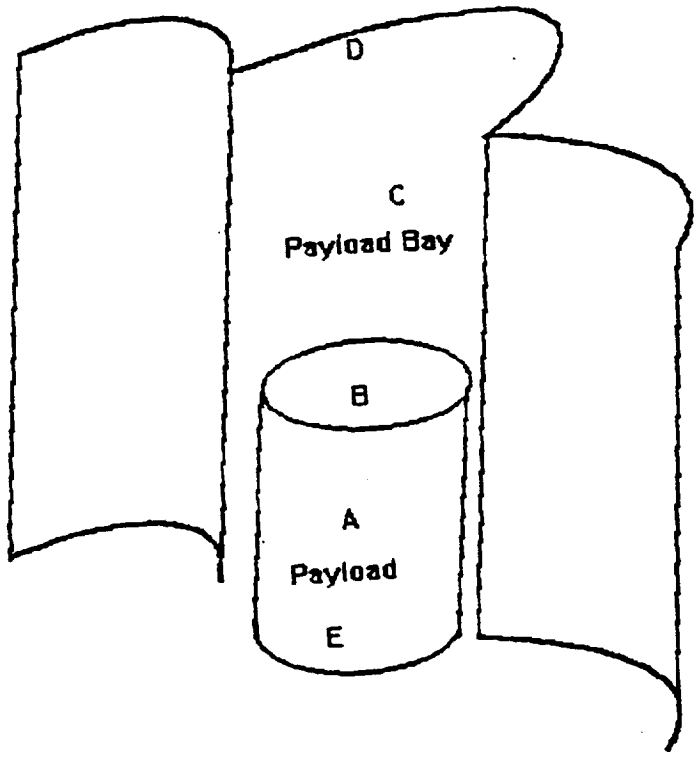

Selected Locations

A – 19.6 A/m

B – 11.7 A/m

C – 6.7 A/m

D – 60.5 A/m

E – 20.1 A/m

Orbiter in Mate Position with the PCR

(Schematic – not-to-scale)

Lightning Attachment to the top of the Catenary

Payload Bay Doors open inside PCR

NSTS Component A Waveform – 200 KA Peak

Figure 6.10 Peak Magnetic Fields Near Payload and in the Payload Bay

The peak magnetic fields are 19.6, 11.7, 6.7, 60.5 and 20.1 A/m for points A to E respectively. For points B, D and E, the waveforms are very similar to waveforms which were previously calculated for points in the PCR which are near to these points and contained in figures 6.6 and 6.7 of the present draft. Points D and E correspond to TOP and BOTTOM curves in figure 6.3. Point B is close to curves in Figure 6.7 for a point interior to the PCR.

On the question about "How good are these results?" it will be useful to obtain some experimental data of response waveforms to a natural lightning strike for comparison to the finite difference calculations. It would be useful also if the loop antennas on top of the PCR could be continuously monitored in the Mate Position to obtain exterior data during a natural lightning strike.

It is expected that the fields will increase from point B in the directions of the upper and lower horizontal inflatable seals located near points D and E respectively. The primary point of entry for electromagnetic coupling appears to be at the upper horizontal inflatable seal. The vertical seals are shielded somewhat by the open PCR Doors. In this case (again, as we will note noted for similar situations in the White Room and PCR in the park position, Chapter 7), it could be very beneficial to have additional grounding straps of various types between the PCR and the Orbiter across the upper and lower horizontal inflatable seals.

CHAPTER 7

CALCULATIONS AT THE ORBITER-WHITE ROOM INTERFACE

7.1 Introduction

For these calculations, the Orbiter is in the Launch position on the Pad as shown in Figure 6.1; the PCR on the RSS is rotated back to the Park position as shown in Figure 4.1. The walkway access to the Orbiter Cabin extends from the Fixed Service Structure (FSS) at the level of the Orbiter Cabin. This walkway terminates at the White Room which interfaces with the Orbiter Cabin. There is an electrically insulating seal between the White Room and the Cabin. Except for the time of the initial contact, there is a grounding cable about 3 meters long connecting the White Room to the Orbiter. On the floor of the White Room is a Slide or "walk-bridge" about 24 inches wide and 44 inches long which extends into the Orbiter to support personnel access into the Orbiter cabin. This slide is made of metal but is not normally grounded on both ends to the White Room and the Orbiter.

The lightning attachment is at the top of the Catenary Wire which is above and insulated from the FSS. The waveform is taken to be the 1 percent strike shown in the NSTS Component A waveform [11] (See also Figure 6.4). It should be noted that this does not represent a direct lightning attachment to any part of the Orbiter or Launch Pad structure. All the direct lightning current is going down the catenary cable to north and south grounding points about 1,000 feet from the FSS. All currents and voltages calculated result from currents which are induced by the time-varying electromagnetic fields emanating from the lightning channel and the catenary wire.

7.2 Calculated Responses

Voltages were calculated between the Orbiter and White Room for the Orbiter in the Launch position with the PCR removed. Various grounding configurations were investigated for a NSTS Component A Lightning Strike to the top of the catenary wire.

Figure 7.1 shows the comparison between no grounding and the 3-meter (10-foot) ground cable connected between the White Room and the Orbiter. For this case we see there is approximately a 5-fold decrease in the voltage between the Orbiter and White Room when the ground cable is connected, i.e., from about 100 KV to about 20 KV peak voltages.

Figure 7.2 shows the comparison between the 3-meter ground cable and a shorter, 2-meter ground cable. We see there is about a 1/3 reduction in voltage for the shorter cable.

Figure 7.3 shows the comparison between the 3-meter ground cable and a case where there are, additionally, grounding connections on the metal walk-bridge between the Orbiter and the White Room. We see there is another 5-fold decrease in the Orbiter-White Room voltage to about 4 KV peak voltage.

Figure 7.4 shows currents on the grounding cable for the various cases. The peak current is similar, about 800 A, for both the 3-meter and 2-meter ground cables. The current is reduced to about 100 A for the case where the walk-bridge is grounded on both sides. In this case the bridge provides a low inductance path between the Orbiter and White Room which is presumably carrying the bulk of the current.

In the Mate Position, a sheet metal surface spanning the gap between the Orbiter Bay and the PCR floor, and grounded on both sides of the gap, could greatly reduce currents and voltages, due to lightning, on any existing drag-on cables between the Orbiter payload and the PCR interior.

Figure 7.5 shows the Orbiter-White Room voltage comparisons between the Mate position and PCR-RSS absent. This case shows some shielding can occur by the presence of the PCR.

It is observed in Figures 7.1 through 7.5 that there are strong resonance oscillations on the order of 1-2 MHz and higher, in both the current and voltage waveforms at the interface. The observed oscillations are due to structural resonances of the larger parts of the launch pad structure. For example, there is a large loop formed by the Orbiter Cabin walkway, the FSS, the Launch Pad and the Orbiter-Solid Rocket Booster assembly; the weak link in this loop is the Orbiter-White Room interface where the calculations have been made. This loop will have a resonance frequency on the order of 1 MHz. Resonance reflections can also occur at places where there is a large dissimilarity in the size and shape of the structural elements; for example, the connection of the walkway with the FSS and the connection interface of the Launch Pad and the Solid Rocket Boosters. The existence of resonances could provide an additional hazard or threat if there are assets such as cables, electronics, or personnel which may have components which could resonate in sympathy with the driving oscillations. It is noted that all of these effects are indirect inductive effects and do not represent, in this case, any direct conduction of the main lightning current.

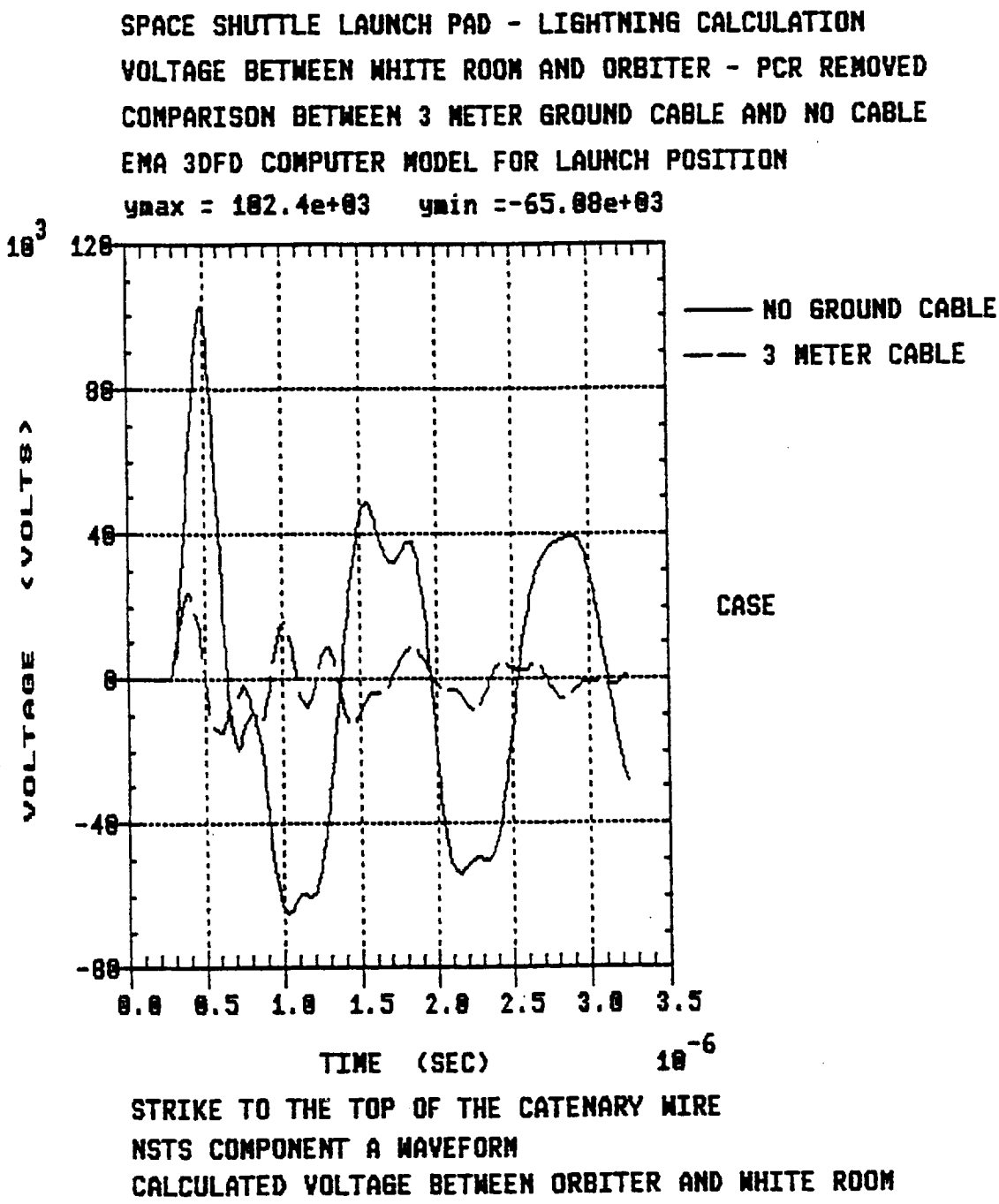

Figure 7.1 **Voltage Between Orbiter and White Room Showing the Effect of a Single Ground Cable Connecting the Orbiter and White Room**

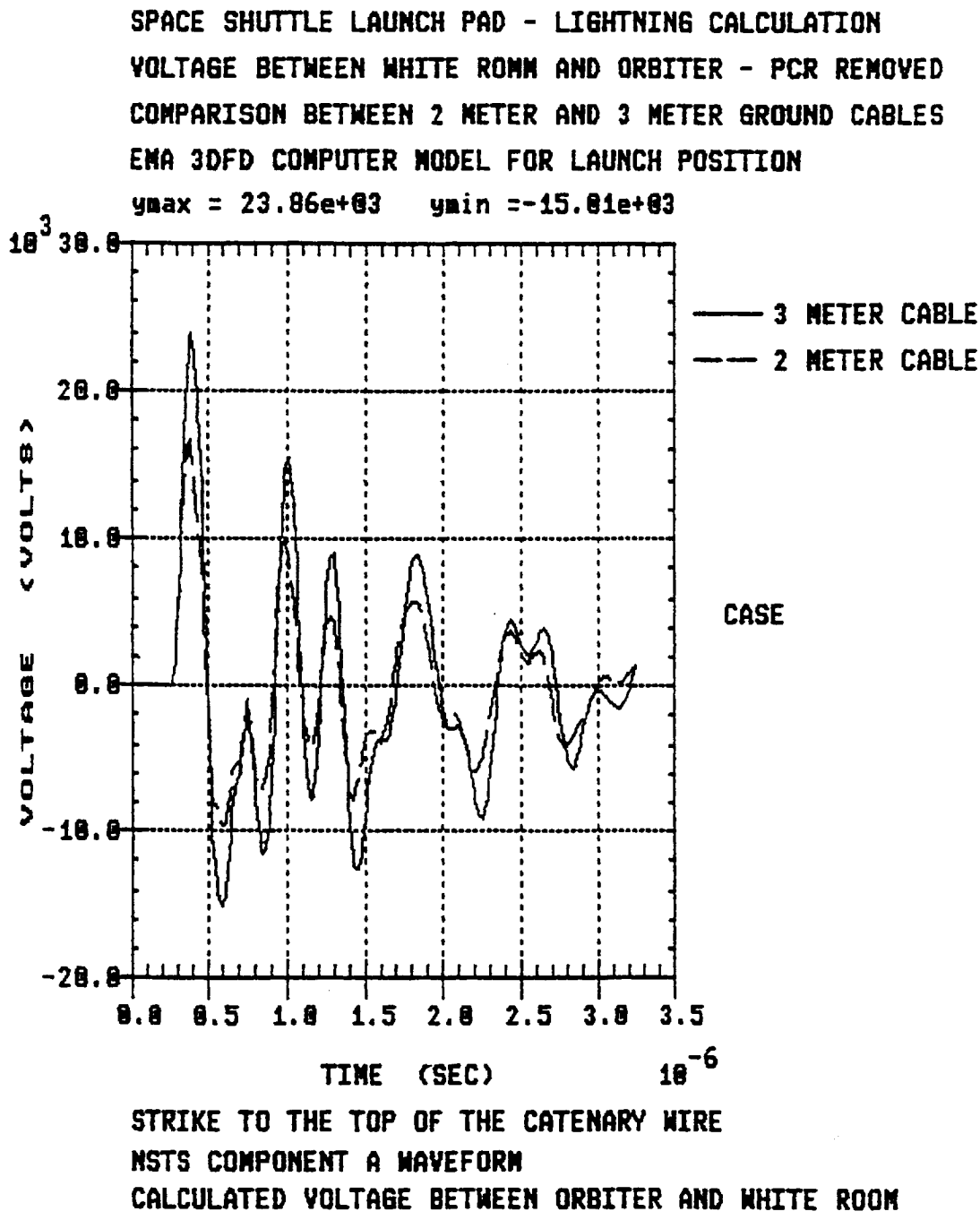

Figure 7.2 **Voltage Between Orbiter and White Room Showing the Effect of Ground Cable Length**

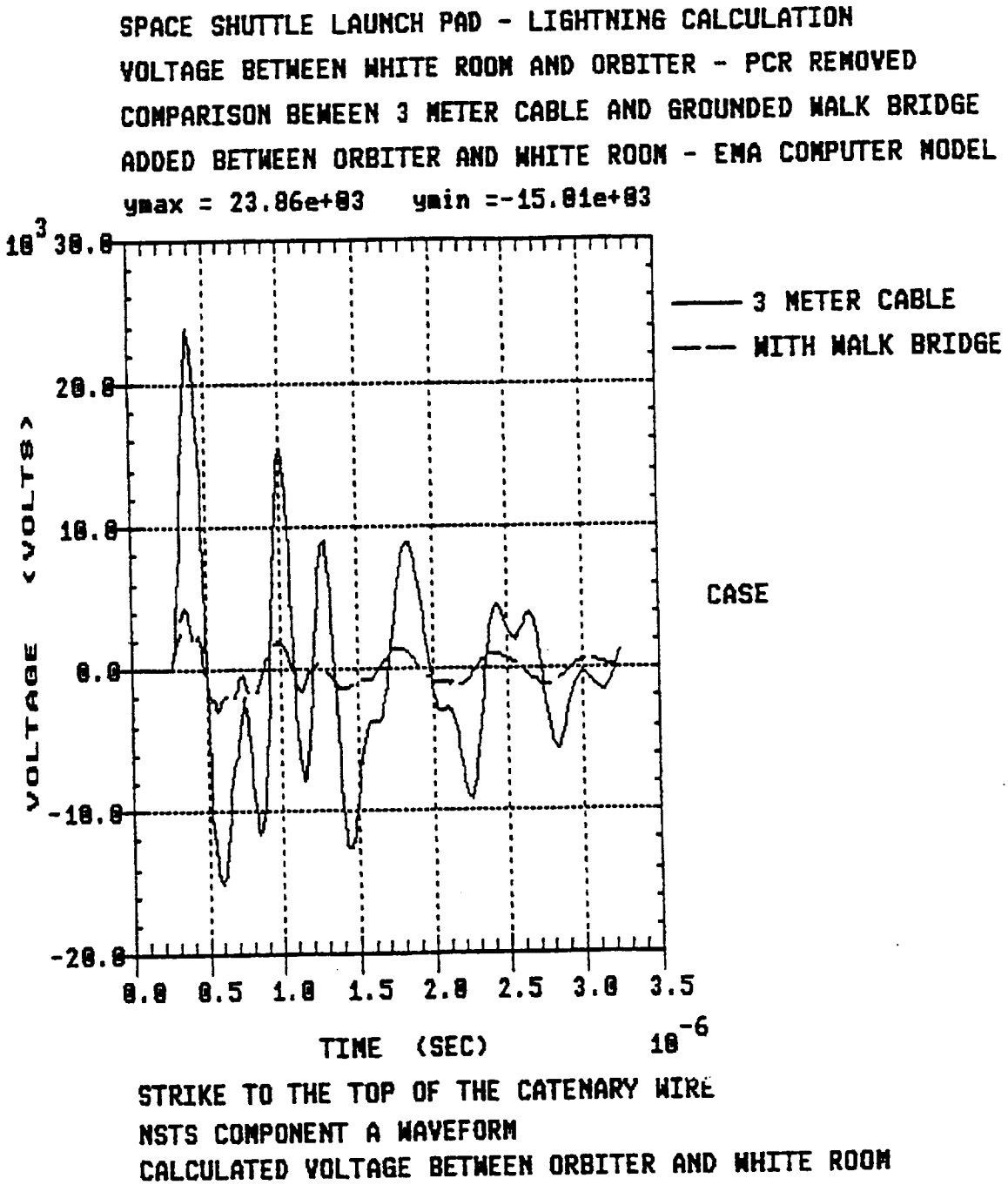

Figure 7.3 **Voltage Between Orbiter and White Room Showing the Difference Between a Single Ground Cable and a Connected Walk Bridge.**

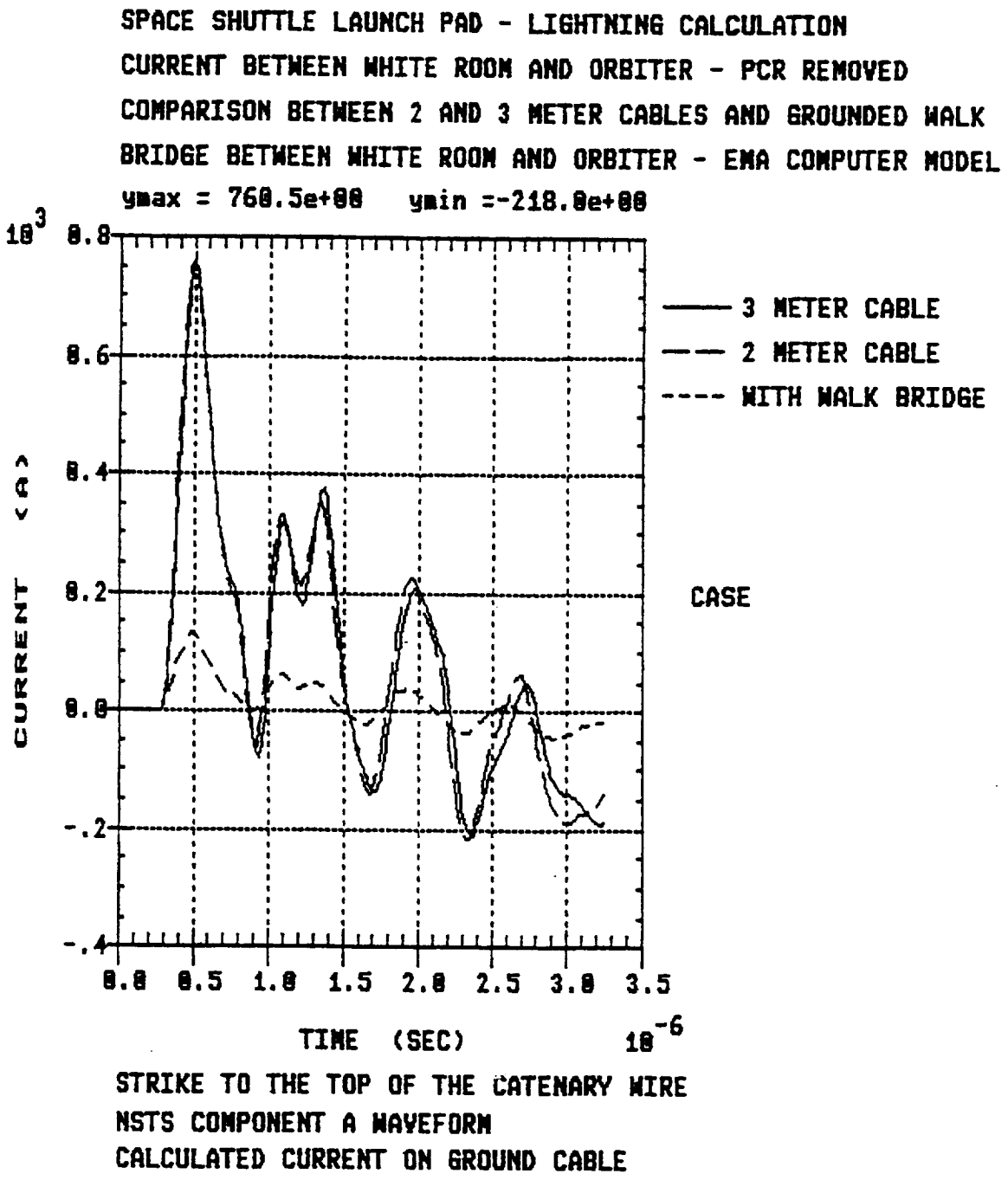

Figure 7.4 **Current on the Ground Cable Between White Room and Orbiter Under Various Grounding Conditions**

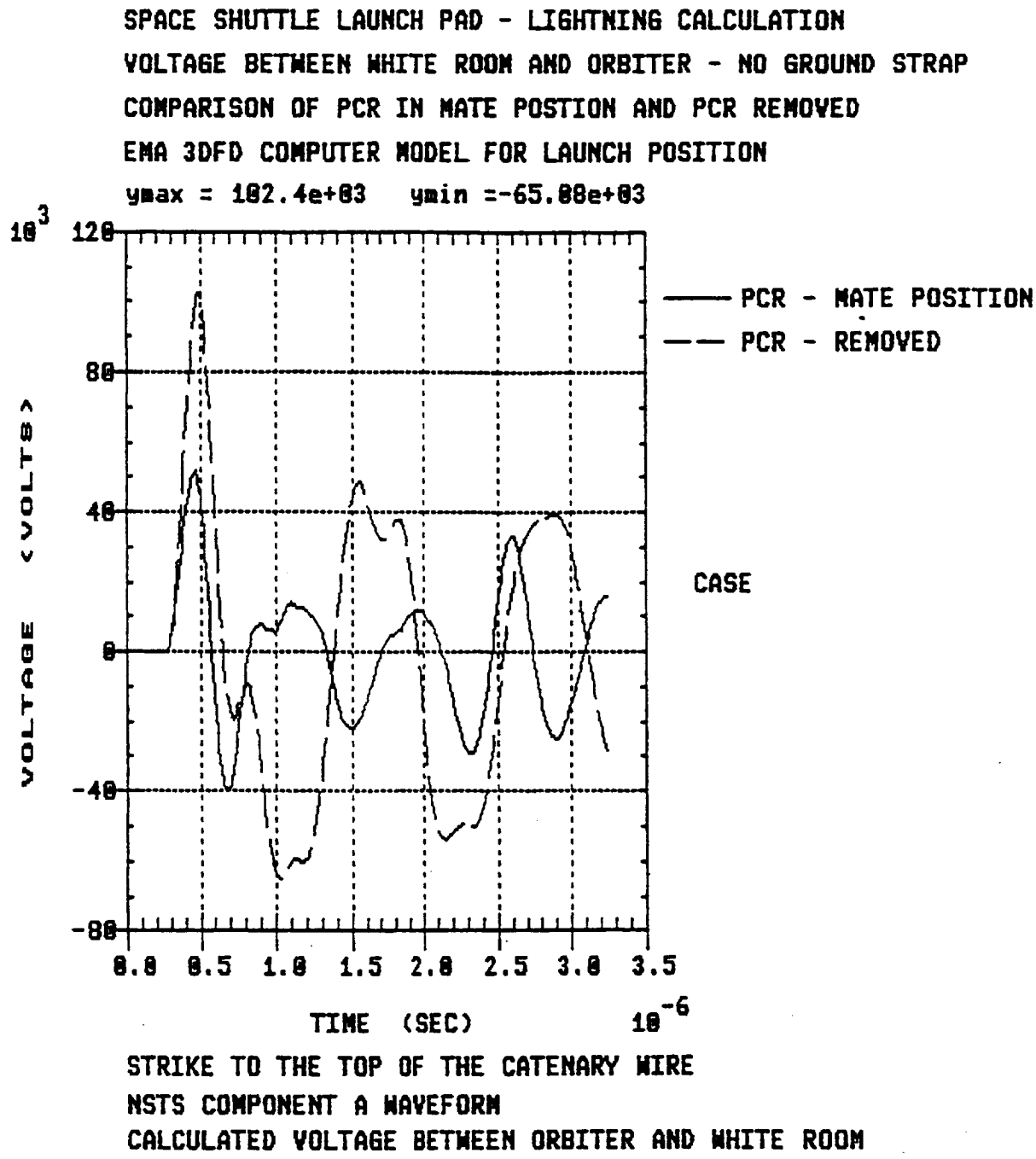

Figure 7.5 **Voltage Between Orbiter and White Room Showing the Difference Between the Mating and Non-Mating of the PCR**

CHAPTER 8

FREQUENCY RESPONSE - TRANSFER FUNCTIONS

The test point responses of the previous chapters show strong resonance responses which are directly tied to the spectral frequency content of the input waveforms including simulated and natural lightning waveforms. The resonance characteristics are due to the size and geometrical extent of the Launch Pad structure. In general, the fundamental resonance frequencies decrease with increasing physical size of the metal object. The lightning response of the Space Shuttle Launch Pad structure is unique in lightning response because of the large size of the structure. For the sizes of various components involved, the resonance frequencies are low enough to be excited by the normal frequency components found in natural lightning, and also in lightning test and standard waveforms.

The general effect of the resonance is to increase the coupling at these frequencies between the catenary wire currents and the induced fields and currents at various points in and around the PCR and the Launch Pad structure. These frequencies show up as relatively high amplitude oscillations superimposed on the direct response waveform; the primary effect of interest is the coupling of the resonance frequencies to the interior of the PCR where they could possibly impact the coupling of energy to elements of the Orbiter Payload.

The resonance response is detected and analyzed by taking Complex Fourier Transforms of the response, F(R), at various test points and by displaying the amplitude and phase of F(R) Transforms obtained from experimental data F(Re) and the Transform as obtained from finite difference calculations F(Rc). The response amplitudes at the resonance frequencies are highly dependent on damping factors which are primarily due to radiation and presence of resistive material in and around the metal structure. The radiation losses are automatically built into the finite difference calculations but the resistive material, if any, has to be directly included into the model.

Complex frequency dependent Transfer Functions, T, may be built from the ratio of the Transform of the Response to the transform of the Source Current waveform, $T = F(R)/F(S)$. The transfer functions can be experimental, $Te = F(Re)/F(Se)$, or calculated from the finite difference model, $Tc = F(Rc)/F(Sc)$. The Transfer function allows the response to be predicted for arbitrary

input source waveforms, Sa. The predicted response, Ra, to Sa is given by Ra=IF(T*F(Sa)) where IF is the Inverse Fourier Transform of the complex product of T with the Fourier Transform of the arbitrary current source waveform, F(Sa). T can be based on calculated data, Tc, or experimental data, Te. The comparison of these two is of interest. The transfer functions must be calculated for each desired test point and must be re-calculated for any changes in geometry, including relevant changes in the attach point of lightning. The transfer functions can be very useful in evaluating and extending data which may be obtained from experiments associated with natural lightning events. The transfer functions can also extend experimental test point data to predict results from natural lightning and standard waveforms.

CHAPTER 9

CONCLUSIONS AND RECOMMENDATIONS

It has been demonstrated that the 3-dimensional finite difference method 3DFD can be used to simulate the lightning environment in and around the Space Shuttle Launch Pad. Two major purposes may be accomplished using this method:

1. Calculate maximum threat levels in critical locations due to a lightning strike. These calculations may be performed under a variety of conditions including lightning attach point, amplitude and waveform, and under various system geometries. The primary output of this activity is to furnish threat data to payload designers such that various mitigation procedures may be considered for the protection of payload components. The effect of various shielding and grounding mitigation techniques may also be evaluated.

2. For natural lightning strikes, extrapolate and integrate data from various measurement observation stations to calculate the responses in critical locations. The observations may come from TV monitors, CWLIS current measurements at each end of the catenary wire, COOPS data, loop antennas on the PCR roof and portable waveform analyzers set out at particular locations. The purpose of this activity is to furnish appropriate date to payload contractors should a lightning attachment occur. This data will assist in determining if additional testing of payload components will be necessary if a lightning attachment should occur during payload installation.

It is expected that additional experimental data is necessary to evaluate and refine model accuracy. Recently developed portable magnetic field waveform analyzers for passive emplacement in and around the PCR, should provide useful data from natural lightning events. Extrapolations of this data, both in waveform and location may be provided by the improved models.

In evaluating the lightning threat, it is important to investigate the effects of the lightning attach point, the Points of Entry (POE's) which may be important, and also the effect of lightning waveform and risetime. Direct amplitude of the waveform is only one factor in determining the amplitude of the response.

Many examples have demonstrated the effect of waveform on the excitation of system resonance oscillations. Evaluation of the source and possible damping mechanisms for these resonances have yet to be evaluated. Transform methods need to be developed and tested to directly effect waveform and location extrapolations without the need for expensive computer time and resources for individual calculation of these effects.

It was shown in the cases of the White Room and the PCR horizontal seams, that additional ground straps, shorter ground straps and low inductive ground straps can greatly reduce gap voltages to the interior spaces.

10.0 REFERENCES

1. Merewether, D. E., and R. Fisher, "Finite Difference Solution of Maxwell's Equations for EMP Applications," EMA 79-R-4, Final Revision, 1/15/82.

2. Mur, G., "Absorbing Boundary Conditions for the Finite Difference Approximations of the Time-Domain Electromagnetic-Field Equations," IEEE Trans. EMC, EMC-23, 4, pp. 377-382, November 1981.

3. Fisher, F. A., R. A. Perala, and J. A. Plumer, "Lightning Protection of Aircraft," published by Lightning Technologies, Inc., 1990.

4. Dalke, R. A., "Parameterization of HEMP coupling Through Apertures in Nested Enclosures as a Function of Aperture Size, Incident Polarization, and Enclosure Size," EMA-87-R-11, March 1988.

5. Eckhoff, A., F. A. Fisher, P. Medelius, Nguyen, and G. Thomas, "Lightning Induced Electromagnetic Environment of the Space Shuttle Payload Changeout Room-Measuring," pp. 407-16, 16th International Aerospace and Ground Conference on Lightning and Static Electricity, May 24, 1994, Mannheim, Germany.

6. Collier, R. S., and F. A. Fisher, "Lightning Induced Electromagnetic Environment of the Space Shuttle Payload Changeout Room-Modeling," pp. 417-26, 16th International Aerospace and Ground Conference on Lightning and Static Electricity, Mannheim, Germany, May 24, 1994.

7. Fisher, F. A., "Study of Lightning Effects at the Payload Changeout Room (PCR)," Lightning Technologies, Inc. report, 20 May 1992.

8. Collier, R. S., and Dr. G. Thomas, "Finite Difference Calculations of Lightning Effects at the Space Shuttle Launch Pad," 1995 International Aerospace and Ground Conference on Lightning and Static Electricity, 26-28 September 1995, Williamsburg, VA.

9. Leteinturier, C., J. H. Hamelin, and André Eybert-Berard, "Submicrosecond Characteristics of Lightning Return-Stroke Currents," IEEE Trans. EMC 33:4, November 1991.

10. Leteinturier, C., C. Weidman, and J. Hamelin, "Current and Electric Field Derivatives in Triggered Lightning Return Strokes," Journal of Geophysical Research 95:D1, pp. 811-828, January 20, 1990.

11. "Space Shuttle Lightning Protection, Test and Analysis Requirements," NSTS 07636.